Optoelectronic properties of multiple quantum barriers nano-scale avalanche photo diodes

Somrita Ghosh

Department of Electronics and Communication Engineering,
Supreme Knowledge Foundation Group of Institutions,
Mankundu, Hooghly, WB – 712139, India
Email: somrita.ghosh@skf.edu.in

Arindam Biswas

Department of Mining Engineering,
Kazi Nazrul University,
Asansol, Burdwan, WB – 713340, India
Email: mailarindambiswas@yahoo.co.in

Aritra Acharyya*

Department of Electronics and Communication Engineering,
Cooch Behar Government Engineering College,
Harinchawra, Ghughumari, WB – 736170, India
Email: ari_besu@yahoo.co.in
*Corresponding author

Abstract: The important optoelectronic properties like spectral response, excess noise characteristics, time and frequency response of multiple quantum barrier (MQB) nano-scale avalanche photodiodes (APDs) based on Si~3C-SiC material system have been studied. A self-consistent simulation method based on quantum drift-diffusion model has been presented. Simulation results show that the Si~3C-SiC MQB nano-APDs are capable of detecting significantly longer wavelengths as compared to infrared flat Si APDs. The multiplication gain and excess noise factor (ENF) of the MQB APDs have been calculated by varying the number of quantum barriers (QBs). The numerically calculated ENF values of MQB APDs have been compared with the ENF of Si flat conventional APDs of similar dimensions and it is observed that the use of QBs leads to significant reduction in ENF of the APDs. Simulation results also show that MQB nano-APDs possess significantly faster time response and wider frequency response as compared to the Si counterparts.

Keywords: avalanche photodiode; APD; multiple quantum barrier; MQB; photocurrent; quantum well; spectral response; excess noise; time and frequency response.

Reference to this paper should be made as follows: Ghosh, S., Biswas, A. and Acharyya, A. (2020) 'Optoelectronic properties of multiple quantum barriers nano-scale avalanche photo diodes', *Int. J. Nanoparticles*, Vol. 12, Nos. 1/2, pp.73–111.

Biographical notes: Somrita Ghosh is presently carrying out her Doctoral research at the Kazi Nazrul University, Asansol, Burdwan, WB India. Her research interests are high frequency semiconductor devices.

Arindam Biswas received his BTech and MTech from the Dumkal Institute of Engineering and Technology, WB, India, and Institute of Radio Physics and Electronics, University of Calcutta, in 2007 and 2010 respectively. Finally he obtained his PhD from the National Institute of Technology, Dugapur, WB, India, in 2013. His research interests are nonlinear optics and high frequency semiconductor devices.

Aritra Acharyya received his BE and MTech from the IIEST, Shibpur, India, and Institute of Radio Physics and Electronics, University of Calcutta, India, in 2007 and 2010 respectively. Finally he obtained his PhD from the Institute of Radio Physics and Electronics, University of Calcutta, in 2016. His research interests are high frequency semiconductor devices. He has already published more than 135 research papers in peer reviewed journals and conference proceedings.

This paper is a revised and expanded version of a paper entitled 'Si~3C-SiC multiple quantum barrier high speed, wide-band avalanche photodiodes' presented at IEEE EDKCON 2018, Kolkata, West Bengal, India, 24th–25th November 2018.

1 Introduction

The avalanche photodiodes (APDs) are the most important and extremely popular photodetectors for fibre optic and free space optical communication systems (Masudy-Panah et al., 2009; Masudy-Panah and Moravvej-Farshi, 2010; Masudy-Panah, 2011; Masudy-Panah and Tikkiwal, 2015). The APDs are generally preferred over all other photodetector types as the primary element in optical receivers in order to convert the optical data into its electrical equivalent. The APDs are generally preferred over all other photodetector types as the primary element in optical receivers in order to convert the optical data into its electrical equivalent. High inherent optical gain, high sensitivity and high speed of APDs are the foremost cause of their extensive popularity. The applications of APDs are not only limited to the optical communication systems; APDs are also used for particle detection, astronomical observations, optical range finding, ultra-sensitive fluorescence, biomedical applications, environmental protection, automated process control, military applications, scintillation detection of nuclear radiation, etc. (Wêgrzecka et al., 2004; Othman et al., 2004; Yang et al., 2003; Britvitch et al., 2004; Renker, 2002; Pansarat, 1997). Since the dimension of the optoelectronic devices used in the optoelectronic integrated circuits (OEICs) has been scaled down to sub-micron to nano-meter range due to the extensive advancement in fabrication technology in modern days, the use of nano-APDs are very common now-a-days (Uemura et al., 2006; Joo et al., 2005; Chen et al., 2013; Pan et al., 2014; Assefa et al., 2010; Youn et al., 2015). Since last two decades, multi-quantum well (MQW) APDs have attracted the attention of the researchers for long wave length detection especially suitable of deep space applications (Wang et al., 2018; Kandaswam et al., 2009; Fissel et

al., 2001; Dong et al., 2016; Brennan and Haralson, 2000). Recently, in 2017, the authors have reported that the problem of high dark current in nano-APDs can be eliminated in a significant extent by using multiple quantum barriers (MQBs) within the intrinsic layer of the device (Acharyya and Ghosh, 2017). However, the authors also admitted that the use of MQB structure may cause significant deterioration in the sensitivity of the device (Acharyya and Ghosh, 2017) at the operating wavelength which is not desirable for reliable nano-photonic applications. Therefore, it is essential to verify that how much extent the dark current of the device can be suppressed by using MQB structure without significant deterioration in the sensitivity. In this paper, a comprehensive model developed by the authors has been used to study the spectral response characteristics of MQB nano-APDs under a wide range of the wavelength of optical illumination. The MQB nano-APDs having n^+-i-p^+ structure based on Si~3C-SiC material system have been simulated to investigate the current-voltage (I-V) characteristics and spectral-response characteristics under different biasing conditions as well as different illumination configurations. The structural parameters of the device, i.e., the dimensions of both the widths of quantum wells (QWs) made of narrower bandgap material Si ($E_g^{(Si)} = 1.12$ eV at 300 K) and quantum barriers (QBs) made of wider bandgap material 3C-SiC ($E_g^{(3C-SiC)} = 2.36$ eV at 300 K) have been appropriately chosen and the number of required QBs have been varied subject to achieve minimum dark current along with most favourable spectral response.

The excess noise characteristics of MQB nano-APDs based on Si~3C-SiC heterostructures have also been studied. It has already been verified in this paper that the better gain and spectral response characteristics of Si~3C-SiC MQB APDs are obtained when the light energy of some intensity of a particular wavelength (λ) is illuminated through p^+-side (ITPS) of the n^+-π-p^+ structured device as compared to when the light energy same intensity and same wavelength is illuminated through n^+-side (ITNS). Therefore, the ITPS configuration is the automatic choice among ITPS and ITNS, especially for the applications related to very low light detection such as deep space astronomy, long-haul fibre-optic communication, etc. The excess noise factor (ENF) as a function of average multiplication gain of Si flat nano-APD and Si~3C-SiC MQB nano-APDs have been calculated for different number of QBs for confirming the superior noise performance of MQB APDs as compared to their flat conventional APD counterpart.

The authors have also investigated the time and frequency responses of the Si~3-SiC MQB nano-APDs and the results have been compared with flat Si APD under similar operating conditions. The diodes are assumed to be reverse biased with 9 V voltage source, just below their corresponding breakdown voltages. It has already been observed in the earlier studies that better optical gain and spectral response of Si~3-SiC MQB nano-APDs are obtained in illumination through p^+-side (ITPS) configuration than the illumination through n^+-side (ITNS) configuration. Therefore, the ITPS configuration is the automatic choice for the applications related to low light detection as mention earlier. That is why the studies on the time and frequency responses have been restricted to ITPS configuration only. The one-dimensional (1D) model of the MQB APD structure under ITNS and ITPS configurations have been shown in Figure 1. The entire simulation and numerical computations have been carried out in MATLAB® software.

Figure 1 Vertical and cross-sectional views of the n^+-π-p^+ structured MQB nano-APD (having typically four QBs) under optical, (a) illumination through n-side (ITNS) (b) illumination through p-side (ITPS) via appropriate optical window

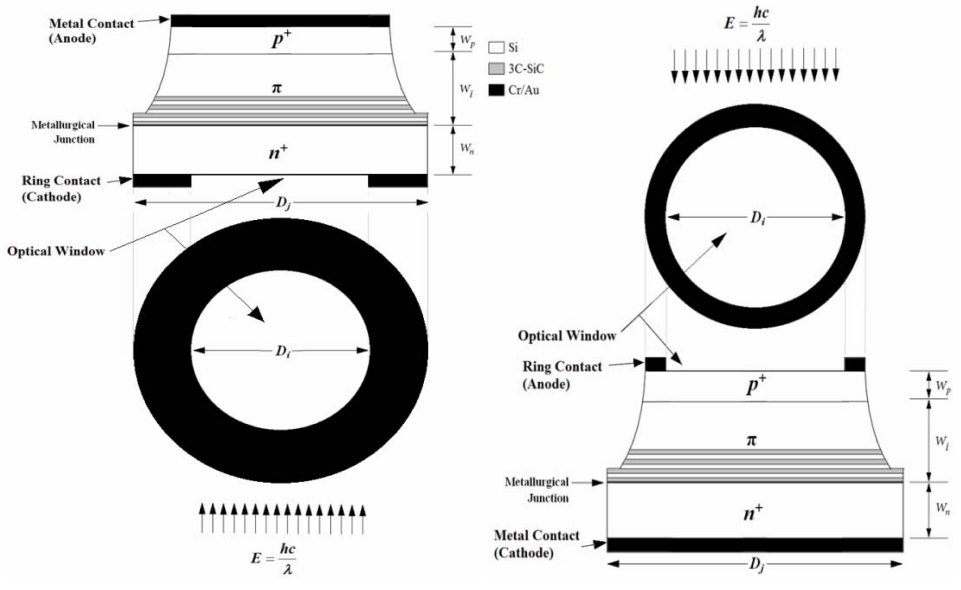

Notes: D_i and D_j are the effective diameter of the opening of optical window and the junction diameter respectively; corresponding areas are $A_i = \pi(D_i/2)^2$ and $A_j = \pi(D_j/2)^2$ respectively.

2 The device structure

The MQB nano-APD is fundamentally a p^+-i-n^+ structure having an intrinsic layer sandwiched between two highly doped p^+ and n^+-layers. The acceptor and donor concentration of the p^+- and n^+-layers respectively are very high ~10^{25} m^{-3} (i.e., $N_D = N_A = 5.0 \times 10^{25}$ m^{-3}) and their widths are chosen to be very thin $W_n = W_p = 25$ nm in order to reduce the diffusion current for improving the impulse response in order to achieve high operating speed. Growth of absolute intrinsic layer over n^+-substrate is not technologically feasible (Acharyya and Ghosh, 2017). That is why i-layer has been considered as slightly p-type and the corresponding acceptor concentration within that layer (N_i) has been taken to be ~10^{21} m^{-3} ($N_i = 10^{21}$ m^{-3}); therefore this layer is nothing but a π-layer and its thickness is chosen to be $W_i = 100$ nm. The schematic diagrams of a typical n^+-π-p^+ structured MQB APD based on Si~3C-SiC heterojunctions under the optical illumination through both n^+-side (ITNS) and p^+-side (ITPS) have been shown in Figures 1(a) and 1(b). A number of QBs based on 3C-SiC are assumed to be grown starting from n^+-π junction which are equidistant to each other. The thicknesses of 3C-SiC QBs (W_b) and the QWs (W_w) based on Si in between two consecutive QBs are

taken to be 5.0 nm; therefore the ration W_b/W_w is always kept fixed at 1.0. Number of 3C-SiC QBs are varied in between $N_b = 1 - 5$; whereas the number of Si QW layers is $N_w = (N_b - 1)$. The MQB APD structure considered for study in this paper may be fabricated via molecular beam epitaxy (MBE) technique (Arthur, 2002). The metal contact from n^+-layer may be deposited via sputter deposition of Cr and Au respectively. Cr prevents short circuit breakdown by migration of Au atoms/ions inside the device at higher temperature across the junction. A controlled optical window can be realised by the ring contact by depositing of Cr and Au respectively on n^+-layer for ITNS or on p^+-layer for ITPS via a special technique (Vyas et al., 1979). Here the effective area of the n^+-π junction is chosen to be A_j = 1,000 nm × 1,000 nm and illumination area is chosen to be A_i = 200 nm × 200 nm.

3 Spectral response

The 1D models of reverse biased MQB nano-APD (having typically four QBs) corresponding to:

a ITNS

b ITPS configurations, associated electric field profiles, energy-band diagrams and illustration of carrier generation characteristics have been shown in Figures 2(a) and 2(b).

The pre-assigned doping profiles associated with ITNS and ITPS configurations are given in the following equations (1) and (2) respectively:

$$\left.\begin{aligned} N(x)\big|_{ITNS} &= N_D && -W_n \le x < 0 \\ &= -N_i && 0 \le x < W_i \\ &= -N_A && W_i \le x < (W_i + W_p) \end{aligned}\right\}$$
$$\left.\begin{aligned} N(x)\big|_{ITPS} &= -N_A && -W_p \le x < 0 \\ &= -N_i && 0 \le x < W_i \\ &= N_D && W_i \le x < (W_i + W_n) \end{aligned}\right\} \qquad (1, 2)$$

Two assumptions have been made at the starting of the theoretical modelling of the structure under consideration; those are:

a widths of the depletion layer in the highly doped n^+- and p^+-regions are much smaller as compared to that in the π-region

b the electric field is uniform at the π-region and zero in n^+- and p^+-regions.

However, those assumptions are not strict, since π-region is not absolutely intrinsic type as mentioned earlier; therefore a very small non-zero slope of electric field is always present there. As long as the impurity concentration in the π-region is very much smaller than the n^+- and p^+-regions, i.e., $|N_D|$, $|N_A| >> |N_i|$, the above-mentioned assumptions are quite justified.

Figure 2 1D models of reverse biased MQB nano-APD (having typically four QBs) corresponding to two different illumination configurations such as, (a) ITNS (b) ITPS, associated electric field profiles, energy-bad diagrams and illustration of carrier generation characteristics

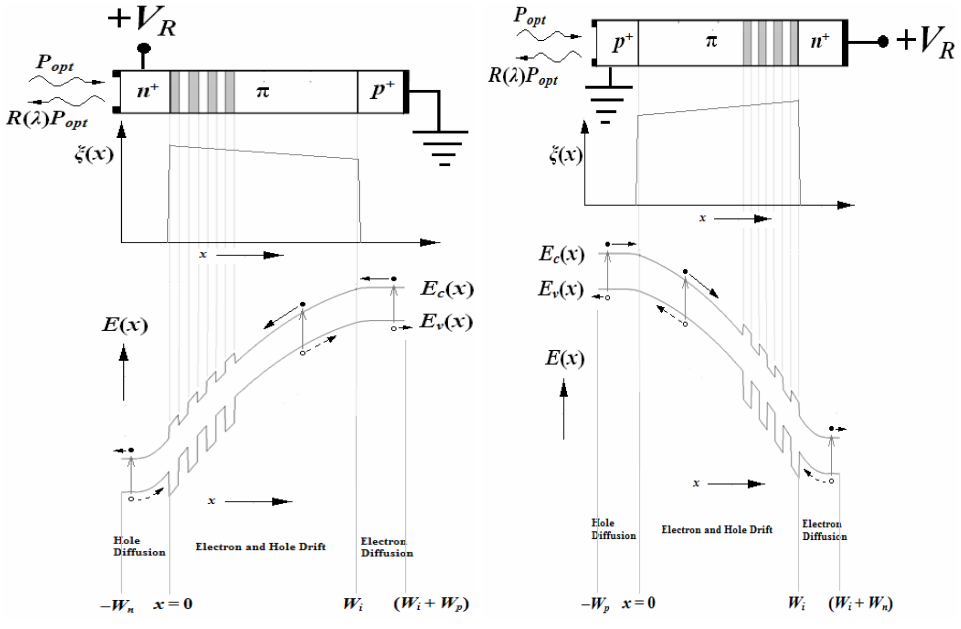

(a) (b)

If the incident optical power be P_{opt} of wavelength λ, then the incident phonon flux density is given by:

$$\Phi_0(\lambda) = \left\{ \frac{P_{opt}\left(1 - R(\lambda)\right)\lambda}{A_i hc} \right\} \tag{3}$$

where h = 6.62 × 10^{-34} J s is the Plank's constant, c = 3.0×10^8 m s^{-1} is the velocity of light at free space, $R(\lambda)$ is the reflectance of the semiconductor surface (here Si) at the cross-sectional surface of either n^+-side or p^+-side, where:

$$R(\lambda) = \left(\frac{n^{(Si)}(\lambda) - n^{(a)}(\lambda)}{n^{(Si)}(\lambda) + n^{(a)}(\lambda)} \right)^2 \tag{4}$$

where $n^{(Si)}(\lambda)$ and $n^{(a)}(\lambda)$ = 1 are the reflective index of Si (Rajkanan et al., 1979; Spitzer and Fan, 1957; Hara and Nishi, 1966) and air respectively at λ.

The electron-hole pair (EHP) generation rate at the space point 'x' within the π-region (i.e., $0 \le x \le W_i$) due to the optical illumination of wavelength λ is given by:

$$G_{r(opt)}^{(drt)}(\lambda, x)\Big|_{ITXS} = \Phi_0(\lambda)\, \alpha(\lambda, x)\, e^{-(\alpha(\lambda,x)x + \alpha_X^{(Si)}(\lambda)W_X)} \tag{5}$$

where $\alpha(\lambda, x)$ is the absorption coefficient at x for the wavelength λ within $0 \le x \le W_i$. The symbol 'r' at the subscript of $G_{r(opt)}^{(drt)}$ denotes either $r \equiv n$ or r $\equiv p$, i.e., either electron

or hole generation rate respectively and the symbol 'X' at the subscript of W_X denotes either $X \equiv n$ or $X \equiv p$, i.e., either W_n for ITNS configuration or W_p for ITPS configuration (thus ITXS denotes either ITNS configuration or ITPS configuration accordingly). Due to the MQB structure of the device, all the material parameters have to be expressed as the function of spatial coordinate 'x' within $0 \le x \le W_i$, i.e.:

$$\left.\begin{aligned} \alpha(\lambda, x) &= \alpha_{r(inb)}^{(Si)}\left(\lambda, \left|N(x)\right|\right) && \Omega_{r(Bulk)}^{(Si)} \\ &= \alpha_{r(insb)}^{(Si)}\left(\lambda, \left|N(x)\right|\right) + \alpha_{r(inb)}^{(Si)}\left(\lambda, \left|N(x)\right|\right) && \Omega_{r(QW)}^{(Si)} \\ &= \alpha_{r(inb)}^{(3C-Si)}\left(\lambda, \left|N(x)\right|\right) && \Omega_{r(Barrier)}^{(3C-SiC)} \end{aligned}\right\}\Bigg|_{T=300K} \tag{6}$$

where $\alpha_{r(inb)}^{(Si)}$ and $\alpha_{r(inb)}^{(3C-SiC)}$ are the r-type (i.e., n- or π- or p-type) absorption coefficients of Si and 3C-SiC respectively at room temperature due to interband transitions in bulk Si and 3C-SiC barrier regions, $\alpha_{r(insb)}^{(Si)}$ is the absorption coefficient associated with the intersubband transitions in Si QWs. The values of $\alpha_{r(inb)}^{(Si)}$ and $\alpha_{r(inb)}^{(3C-SiC)}$ as functions of both λ and doping concentration have been taken in the present calculation from the published experimental reports (Rajkanan et al., 1979; Spitzer and Fan, 1957; Hara and Nishi, 1966; Solangi and Chaudry, 1992), whereas the values of $\alpha_{r(insb)}^{(Si)}$ for different λ for a given carrier density have been calculated by using the method adopted by Mukherjee and Das (2014) and Manasreh (2005). The electron and hole drift photocurrent densities for both ITNS and ITPS configurations can be calculated as:

$$\left.\begin{aligned} J_{r(opt)}^{(drt)}(\lambda)\Big|_{ITNS} &= -q\int_{x=0}^{x=W_i} G_{r(opt)}^{(drt)}(\lambda, x)\Big|_{ITNS}\, dx \\ &= -q\Phi_0(\lambda)e^{-\alpha_{n(inb)}^{(Si)}(\lambda,|N_D|)W_n}\left(\int_{x=0}^{x=W_i}\alpha(\lambda, x)e^{-\alpha(\lambda,x)x}\, dx\right) \\ J_{r(opt)}^{(drt)}(\lambda)\Big|_{ITPS} &= -q\int_{x=0}^{x=W_i} G_{r(opt)}^{(drt)}(\lambda, x)\Big|_{ITPS}\, dx \\ &= -q\Phi_0(\lambda)e^{-\alpha_{p(inb)}^{(Si)}(\lambda,|N_A|)W_p}\left(\int_{x=0}^{x=W_i}\alpha(\lambda, x)e^{-\alpha(\lambda,x)x}\, dx\right) \end{aligned}\right\} \tag{7, 8}$$

where $q = 1.6 \times 10^{-19}$ C is the magnitude of the charge of an electron and hole.

The excess hole and electron densities at n^+- and p^+-regions (i.e., the excess minority carrier densities) due to illumination may be written as:

$$\left.\begin{aligned} \Delta p_n(\lambda, x)\Big|_{ITXS} &= \left(p_n(\lambda, x)\Big|_{ITXS} - p_{n0}\right) \\ \Delta n_p(\lambda, x)\Big|_{ITXS} &= \left(n_p(\lambda, x)\Big|_{ITXS} - n_{p0}\right) \end{aligned}\right\} \tag{9, 10}$$

where $p_n(\lambda, x)$ and $n_p(\lambda, x)$ are the minority hole and electron densities at n^+- and p^+-regions respectively at any space point x for the optical illumination of wavelength λ, p_{n0} and n_{p0} are the corresponding equilibrium values respectively, i.e., $p_{n0} = n_i^{(Si)}/N_D$

and $n_{p0} = n_i^{(Si)} / N_A$, where $n_i^{(Si)}$ is the intrinsic carrier concentration in Si. Now the steady-state continuity equations for a hole in the n^+-region and for an electron in the p^+-region for either ITNS or ITPS can be written as:

$$D_p^{(Si)} \frac{\partial^2 \Delta p_n(\lambda, x)\big|_{ITXS}}{\partial x^2} - \frac{\Delta p_n(\lambda, x)\big|_{ITXS}}{\tau_p^{(Si)}} + G_{p(opt)}^{(diff)}(\lambda, x)\Big|_{ITXS} = 0$$
$$\Rightarrow \begin{Bmatrix} -W_n \le x < 0 & \rightarrow & ITNS \\ W_i \le x \le (W_i + W_n) & \rightarrow & ITPS \end{Bmatrix} \tag{11}$$

$$D_n^{(Si)} \frac{\partial^2 \Delta n_p(\lambda, x)\big|_{ITXS}}{\partial x^2} - \frac{\Delta n_p(\lambda, x)\big|_{ITXS}}{\tau_n^{(Si)}} + G_{n(opt)}^{(diff)}(\lambda, x)\Big|_{ITXS} = 0$$
$$\Rightarrow \begin{Bmatrix} W_i \le x \le (W_i + W_p) & \rightarrow & ITNS \\ -W_p \le x < 0 & \rightarrow & ITPS \end{Bmatrix} \tag{12}$$

where $D_{p,n}^{(Si)}$ and $\tau_{p,n}^{(Si)}$ are the diffusivity and lifetime of holes and electrons in Si; these are related with the diffusion lengths of holes and electrons by the equation $L_{p,n}^{(Si)} = \sqrt{D_{p,n}^{(Si)} \tau_{p,n}^{(Si)}}$ in Si. The hole and electron generation rates in n^+- and p^+-regions respectively in ITNS configuration are given by:

$$G_{p(opt)}^{(diff)}(\lambda, x)\Big|_{ITNS} = \Phi_0(\lambda)\, \alpha_{n(inb)}^{(Si)}\left(\lambda, |N_D|\right) e^{-\alpha_{n(inb)}^{(Si)}(\lambda, |N_D|)x}$$
$$G_{n(opt)}^{(diff)}(\lambda, x)\Big|_{ITNS} = \Phi_0(\lambda)\, \alpha_{p(inb)}^{(Si)}\left(\lambda, |N_A|\right) e^{-\left\{H_1 + \alpha_{p(inb)}^{(Si)}(\lambda, |N_A|)x\right\}} \tag{13, 14}$$

where $H_1 = \alpha_{n(inb)}^{(Si)}(\lambda, |N_D|)W_n + (\alpha_{\pi(insb)}^{(Si)}(\lambda, |N_i|) + \alpha_{\pi(inb)}^{(Si)}(\lambda, |N_i|))N_w W_w + \alpha_{\pi(inb)}^{(3C-SiC)}(\lambda, |N_i|)N_b W_b + \alpha_{\pi(inb)}^{(Si)}(\lambda, |N_i|)(W_i - N_b W_b - N_w W_w)$. Similarly those due to ITPS are given by:

$$G_{p(opt)}^{(diff)}(\lambda, x)\Big|_{ITPS} = \Phi_0(\lambda)\, \alpha_{n(inb)}^{(Si)}\left(\lambda, |N_D|\right) e^{-\left\{H_2 + \alpha_{n(inb)}^{(Si)}(\lambda, |N_D|)x\right\}}$$
$$G_{n(opt)}^{(diff)}(\lambda, x)\Big|_{ITPS} = \Phi_0(\lambda)\, \alpha_{p(inb)}^{(Si)}\left(\lambda, |N_A|\right) e^{-\alpha_{p(inb)}^{(Si)}(\lambda, |N_A|)x} \tag{15, 16}$$

where $H_2 = \alpha_{p(inb)}^{(Si)}(\lambda, |N_A|)W_p + (\alpha_{\pi(insb)}^{(Si)}(\lambda, |N_i|) + \alpha_{\pi(inb)}^{(Si)}(\lambda, |N_i|))N_w W_w + \alpha_{\pi(inb)}^{(3C-SiC)}(\lambda, |N_i|)N_b W_b + \alpha_{\pi(inb)}^{(Si)}(\lambda, |N_i|)(W_i - N_b W_b - N_w W_w)$. The boundary conditions for solving the equations (11) and (12) for ITNS configuration are respectively given in the equations (17) and (18); those are given by:

$$\left.\begin{aligned} & x = -W_n : p_n(\lambda, x = -W_n)\big|_{ITNS} = p_n(\lambda, 0)\big|_{ITNS} \\ & \Rightarrow \Delta p_n(\lambda, x = -W_n)\big|_{ITNS} = \left(p_n(\lambda, 0)\big|_{ITNS} - p_{n0}\right) \end{aligned}\right\}$$
$$\left.\begin{aligned} & x = 0 : p_n(\lambda, x = 0)\big|_{ITNS} = 0 \\ & \Rightarrow \Delta p_n(\lambda, x = 0)\big|_{ITNS} = -p_{n0} \end{aligned}\right\} \tag{17}$$

$$\left.\begin{aligned} &x = W_i : n_p\left(\lambda, x = W_i\right)\big|_{ITNS} = 0 \\ &\Rightarrow \Delta n_p\left(\lambda, x = W_i\right)\big|_{ITNS} = -n_{p0} \end{aligned}\right\} \\ \left.\begin{aligned} &x = \left(W_i + W_p\right) : n_p\left(\lambda, x = \left(W_i + W_p\right)\right)\big|_{ITNS} = n_p(\lambda, 0)\big|_{ITNS} \\ &\Rightarrow \Delta n_p\left(\lambda, x = \left(W_i + W_p\right)\right)\big|_{ITNS} = \left(n_p(\lambda, 0)\big|_{ITNS} - n_{p0}\right) \end{aligned}\right\} \tag{18}$$

Similarly the boundary conditions for solving the equations (11) and (12) for ITPS configuration are respectively given in the equations (19) and (20); those are given by:

$$\left.\begin{aligned} &x = W_i : p_n\left(\lambda, x = W_i\right)\big|_{ITPS} = 0 \\ &\Rightarrow \Delta p_n\left(\lambda, x = W_i\right)\big|_{ITPS} = -p_{n0} \end{aligned}\right\} \\ \left.\begin{aligned} &x = \left(W_i + W_n\right) : p_n\left(\lambda, x = \left(W_i + W_n\right)\right)\big|_{ITPS} = p_n(\lambda, 0)\big|_{ITPS} \\ &\Rightarrow \Delta p_n\left(\lambda, x = \left(W_i + W_n\right)\right)\big|_{ITPS} = \left(p_n(\lambda, 0)\big|_{ITPS} - p_{n0}\right) \end{aligned}\right\} \tag{19}$$

$$\left.\begin{aligned} &x = -W_p : n_p\left(\lambda, x = -W_n\right)\big|_{ITPS} = n_p(\lambda, 0)\big|_{ITPS} \\ &\Rightarrow \Delta n_p\left(\lambda, x = -W_p\right)\big|_{ITPS} = \left(n_p(\lambda, 0)\big|_{ITPS} - n_{p0}\right) \end{aligned}\right\} \\ \left.\begin{aligned} &x = 0 : n_p(\lambda, x = 0)\big|_{ITPS} = 0 \\ &\Rightarrow \Delta n_p(\lambda, x = 0)\big|_{ITPS} = -n_{p0} \end{aligned}\right\} \tag{20}$$

General solutions of the equations (11) and (12) due to ITNS configuration are given by:

$$\begin{aligned} \Delta p_n(\lambda, x)\big|_{ITNS} &= A_1(\lambda)\big|_{ITNS}\, e^{-\left(\frac{x}{L_p^{(Si)}}\right)} + B_1(\lambda)\big|_{ITNS}\, e^{\left(\frac{x}{L_p^{(Si)}}\right)} \\ &\quad + C_1(\lambda)\big|_{ITNS}\, e^{-\alpha_{n(inb)}^{(Si)}(\lambda, |N_D|)x} \\ \Delta n_p(\lambda, x)\big|_{ITNS} &= A_2(\lambda)\big|_{ITNS}\, e^{-\left(\frac{x}{L_p^{(Si)}}\right)} + B_2(\lambda)\big|_{ITNS}\, e^{\left(\frac{x}{L_p^{(Si)}}\right)} \\ &\quad + C_2(\lambda)\big|_{ITNS}\, e^{-\alpha_{p(inb)}^{(Si)}(\lambda, |N_A|)x} \end{aligned} \tag{21, 22}$$

Now the constants $A_{1,2}$ and $B_{1,2}$ can be obtained from the aforementioned boundary conditions. For ITNS, the constants A_1 and B_1 are obtained by putting the boundary conditions in (17) into the equation (21). Those are obtained as:

$$A_1(\lambda)\big|_{ITNS} = \left\{ \begin{array}{l} p_n(\lambda, 0)\big|_{ITNS} - p_{n0}\left(1 - e^{-\left(\frac{W_n}{L_p^{(Si)}}\right)}\right) \\ \dfrac{-C_1(\lambda)\big|_{ITNS}\left(e^{\alpha_{n(inb)}^{(Si)}(\lambda, |N_D|)W_n} - e^{-\left(\frac{W_n}{L_p^{(Si)}}\right)}\right)}{\left(e^{\left(\frac{W_n}{L_p^{(Si)}}\right)} - e^{-\left(\frac{W_n}{L_p^{(Si)}}\right)}\right)} \end{array} \right\} \tag{23}$$

$$B_1(\lambda)\big|_{ITNS} = \left\{ \begin{array}{l} -p_n(\lambda,0)\big|_{ITNS} + p_{n0}\left(1-e^{\left(\frac{W_n}{L_p^{(Si)}}\right)}\right) \\ \dfrac{+C_1(\lambda)\big|_{ITNS}\left(e^{\alpha_{n(inb)}^{(Si)}(\lambda,|N_D|)W_n} - e^{\left(\frac{W_n}{L_p^{(Si)}}\right)}\right)}{\left(e^{\left(\frac{W_n}{L_p^{(Si)}}\right)} - e^{-\left(\frac{W_n}{L_p^{(Si)}}\right)}\right)} \end{array} \right\} \tag{24}$$

Similarly, the constants A_2 and B_2 are obtained by putting the boundary conditions in (18) into the equation (22). Those are obtained as:

$$A_2(\lambda)\big|_{ITNS} = \left\{ \begin{array}{l} -n_p(\lambda,0)\big|_{ITNS} + n_{p0}\left(1-e^{\left(\frac{W_p}{L_n^{(Si)}}\right)}\right) \\ \dfrac{-C_2(\lambda)\big|_{ITNS}\, e^{-\alpha_{p(inb)}^{(Si)}(\lambda,|N_A|)W_i}\left(e^{\left(\frac{W_p}{L_n^{(Si)}}\right)} - e^{-\alpha_{p(inb)}^{(Si)}(\lambda,|N_A|)W_p}\right)}{e^{-\left(\frac{W_i}{L_n^{(Si)}}\right)}\left(e^{\left(\frac{W_p}{L_n^{(Si)}}\right)} - e^{-\left(\frac{W_p}{L_n^{(Si)}}\right)}\right)} \end{array} \right\} \tag{25}$$

$$B_2(\lambda)\big|_{ITNS} = \left\{ \begin{array}{l} n_p(\lambda,0)\big|_{ITNS} - n_{p0}\left(1-e^{-\left(\frac{W_p}{L_n^{(Si)}}\right)}\right) \\ \dfrac{+C_2(\lambda)\big|_{ITNS}\, e^{-\alpha_{p(inb)}^{(Si)}(\lambda,|N_A|)W_i}\left(e^{-\left(\frac{W_p}{L_n^{(Si)}}\right)} - e^{-\alpha_{p(inb)}^{(Si)}(\lambda,|N_A|)W_p}\right)}{e^{\left(\frac{W_i}{L_n^{(Si)}}\right)}\left(e^{\left(\frac{W_p}{L_n^{(Si)}}\right)} - e^{-\left(\frac{W_p}{L_n^{(Si)}}\right)}\right)} \end{array} \right\} \tag{26}$$

The constants C_1 and C_2 for ITNS can be obtained by calculating $\partial^2\Delta p_n/\partial x^2$ and $\partial^2\Delta n_p/\partial x^2$ from equations (21) and (22) respectively and then putting those double derivatives as well as Δp_n and Δn_p from equations (21) and (22) in equations (11) and (12) respectively. Those are obtained as:

$$\begin{aligned} C_1(\lambda)\big|_{ITNS} &= \left[\frac{\Phi_0(\lambda)\alpha_{n(inb)}^{(Si)}\left(\lambda,|N_D|\right)\left(L_p^{(Si)}\right)^2}{D_p^{(Si)}\left\{1-\left(\alpha_{n(inb)}^{(Si)}\left(\lambda,|N_D|\right)\right)^2\left(L_p^{(Si)}\right)^2\right\}}\right] \\ C_2(\lambda)\big|_{ITNS} &= \left[\frac{\Phi_0(\lambda)\alpha_{p(inb)}^{(Si)}\left(\lambda,|N_A|\right)\left(L_n^{(Si)}\right)^2}{D_n^{(Si)}\left\{1-\left(\alpha_{p(inb)}^{(Si)}\left(\lambda,|N_A|\right)\right)^2\left(L_n^{(Si)}\right)^2\right\}}\right]e^{-H_1} \end{aligned} \tag{27, 28}$$

Now, substituting the calculated expressions of $A_{1,2}$, $B_{1,2}$ and $C_{1,2}$ given in equations (23)–(28) in the general solutions given in the equations (21) and (22) and using the relations in the equations (9) and (10), the expressions of $p_n(\lambda, x)$ and $n_p(\lambda, x)$ can be obtained for the ITNS configuration. After simplifications, those expressions can be written as:

$$p_n(\lambda, x)\big|_{ITNS} = p_{n0} + C_1(\lambda)\big|_{ITNS} e^{-\alpha_{n(inb)}^{(Si)}(\lambda,|N_D|)x} + \frac{\left\{\begin{array}{l}\left(p_{n0} - p_n(\lambda, 0)\big|_{ITNS} + C_1(\lambda)\big|_{ITNS} e^{\alpha_{n(inb)}^{(Si)}(\lambda,|N_D|)W_n}\right)\sinh\left(\dfrac{x}{L_p^{(Si)}}\right) \\ -\left(p_{n0} + C_1(\lambda)\big|_{ITNS}\right)\sinh\left(\dfrac{W_n + x}{L_p^{(Si)}}\right)\end{array}\right\}}{\sinh\left(\dfrac{W_n}{L_p^{(Si)}}\right)} \tag{29}$$

$$n_p(\lambda, x)\big|_{ITNS} = n_{p0} + C_2(\lambda)\big|_{ITNS} e^{-\alpha_{p(inb)}^{(Si)}(\lambda,|N_A|)x} + \frac{\left\{\begin{array}{l}\left(\begin{array}{l}n_p(\lambda, 0)\big|_{ITNS} - n_{p0} \\ -C_2(\lambda)\big|_{ITNS} e^{-\alpha_{p(inb)}^{(Si)}(\lambda,|N_A|)(W_i+W_p)}\end{array}\right)\sinh\left(\dfrac{x - W_i}{L_n^{(Si)}}\right) \\ -\left(n_{p0} + C_2(\lambda)\big|_{ITNS}\right)\sinh\left(\dfrac{W_i + W_p - x}{L_n^{(Si)}}\right)\end{array}\right\}}{\sinh\left(\dfrac{W_n}{L_n^{(Si)}}\right)} \tag{30}$$

Therefore, the hole and electron diffusion photocurrent densities in the n^+- and p^+-regions respectively in ITNS configuration can be obtained as:

$$J_{p(opt)}^{(diff)}(\lambda)\big|_{ITNS} = -qD_p^{(Si)}\left.\frac{\partial\, p_n(\lambda, x)\big|_{ITNS}}{\partial x}\right|_{x=0}$$

$$= qD_p^{(Si)}\left[\begin{array}{l}\alpha_{n(inb)}^{(Si)}\left(\lambda, |N_D|\right)C_1(\lambda)\big|_{ITNS} \\ -\left(\dfrac{1}{L_p^{(Si)}\sinh\left(\dfrac{W_n}{L_p^{(Si)}}\right)}\right)\left\{\begin{array}{l}p_{n0}\left(1 - \cosh\left(\dfrac{W_n}{L_p^{(Si)}}\right)\right) \\ +C_1(\lambda)\big|_{ITNS}\left(e^{\alpha_{n(inb)}^{(Si)}(\lambda,|N_D|)W_n} - \cosh\left(\dfrac{W_n}{L_p^{(Si)}}\right)\right) \\ -p_n(\lambda, 0)\big|_{ITNS}\end{array}\right\}\end{array}\right] \tag{31}$$

$$J_{n(opt)}^{(diff)}(\lambda)\big|_{ITNS} = qD_n^{(Si)}\left.\frac{\partial\, n_p(\lambda, x)\big|_{ITNS}}{\partial x}\right|_{x=W_i}$$

$$= -qD_n^{(Si)}\left[\begin{array}{l}\alpha_{p(inb)}^{(Si)}\left(\lambda, |N_A|\right)C_2(\lambda)\big|_{ITNS} e^{-\alpha_{p(inb)}^{(Si)}(\lambda,|N_A|)W_i} \\ +\left(\dfrac{1}{L_n^{(Si)}\sinh\left(\dfrac{W_p}{L_n^{(Si)}}\right)}\right)\left\{\begin{array}{l}n_{p0}\left(1 + \cosh\left(\dfrac{W_p}{L_n^{(Si)}}\right)\right) \\ +C_2(\lambda)\big|_{ITNS}\left(e^{-\alpha_{p(inb)}^{(Si)}(\lambda,|N_A|)(W_i+W_p)} - \cosh\left(\dfrac{W_p}{L_n^{(Si)}}\right)\right) \\ -n_p(\lambda, 0)\big|_{ITNS}\end{array}\right\}\end{array}\right] \tag{32}$$

Now, proceeding in the similar approach, the hole and electron diffusion current densities in the n^+- and p^+-regions respectively in ITPS configuration can also be obtained. Those are given by:

$$J_{p(opt)}^{(diff)}(\lambda)\Big|_{ITPS} = -qD_p^{(Si)} \left.\frac{\partial\, p_n(\lambda, x)\big|_{ITPS}}{\partial x}\right|_{x=W_i}$$

$$= qD_p^{(Si)} \left[\begin{array}{l} \alpha_{n(inb)}^{(Si)}\left(\lambda, |N_D|\right) C_2(\lambda)\big|_{ITPS}\, e^{-\alpha_{n(inb)}^{(Si)}(\lambda,|N_D|)W_i} \\ + \left(\dfrac{1}{L_p^{(Si)} \sinh\left(\dfrac{W_n}{L_p^{(Si)}}\right)}\right) \left\{ \begin{array}{l} p_{n0}\left(1+\cosh\left(\dfrac{W_n}{L_p^{(Si)}}\right)\right) \\ +C_2(\lambda)\big|_{ITPS} \left(\begin{array}{l} e^{-\alpha_{n(inb)}^{(Si)}(\lambda,|N_D|)(W_i+W_n)} \\ -\cosh\left(\dfrac{W_n}{L_p^{(Si)}}\right) \end{array} \right) \\ -\, p_n(\lambda,0)\big|_{ITPS} \end{array} \right\} \end{array} \right] \tag{33}$$

$$J_{n(opt)}^{(diff)}(\lambda)\Big|_{ITPS} = qD_n^{(Si)} \left.\frac{\partial\, n_p(\lambda, x)\big|_{ITPS}}{\partial x}\right|_{x=0}$$

$$= qD_n^{(Si)} \left[\begin{array}{l} \alpha_{p(inb)}^{(Si)}\left(\lambda, |N_A|\right) C_1(\lambda)\big|_{ITPS} \\ -\left(\dfrac{1}{L_n^{(Si)} \sinh\left(\dfrac{W_p}{L_n^{(Si)}}\right)}\right) \left\{ \begin{array}{l} n_{p0}\left(1-\cosh\left(\dfrac{W_p}{L_n^{(Si)}}\right)\right) \\ +C_1(\lambda)\big|_{ITPS} \left(e^{\alpha_{p(inb)}^{(Si)}(\lambda,|N_A|)W_p} - \cosh\left(\dfrac{W_p}{L_n^{(Si)}}\right)\right) \\ -\, n_p(\lambda,0)\big|_{ITPS} \end{array} \right\} \end{array} \right] \tag{34}$$

where the constants C_1 and C_2 for ITPS are given by:

$$C_1(\lambda)\big|_{ITPS} = \left[\frac{\Phi_0(\lambda)\alpha_{p(inb)}^{(Si)}\left(\lambda, |N_A|\right)\left(L_n^{(Si)}\right)^2}{D_n^{(Si)}\left\{1-\left(\alpha_{p(inb)}^{(Si)}\left(\lambda, |N_A|\right)\right)^2\left(L_n^{(Si)}\right)^2\right\}} \right]$$

$$C_2(\lambda)\big|_{ITPS} = \left[\frac{\Phi_0(\lambda)\alpha_{n(inb)}^{(Si)}\left(\lambda, |N_D|\right)\left(L_p^{(Si)}\right)^2}{D_p^{(Si)}\left\{1-\left(\alpha_{n(inb)}^{(Si)}\left(\lambda, |N_D|\right)\right)^2\left(L_p^{(Si)}\right)^2\right\}} \right] e^{-H_2} \tag{35, 36}$$

In case of both ITNS and ITPS configurations, the total hole and electron photocurrent densities can be calculated by adding the corresponding drift and diffusion current components calculated earlier. Those are given by:

$$\left.\begin{array}{l} J_{p(opt)}^{(total)}(\lambda)\big|_{ITXS} = J_{p(opt)}^{(drt)}(\lambda)\big|_{ITXS} + J_{p(opt)}^{(diff)}(\lambda)\big|_{ITXS} \\ J_{n(opt)}^{(total)}(\lambda)\big|_{ITXS} = J_{n(opt)}^{(drt)}(\lambda)\big|_{ITXS} + J_{n(opt)}^{(diff)}(\lambda)\big|_{ITXS} \end{array}\right\} \tag{37, 38}$$

Now, the total photocurrent density is equal to the hole photocurrent density plus the electron photocurrent density. Thus the total photocurrent density is given by:

$$J_{(opt)}^{(total)}(\lambda)\Big|_{ITXS} = J_{p(opt)}^{(total)}(\lambda)\Big|_{ITXS} + J_{n(opt)}^{(total)}(\lambda)\Big|_{ITXS} \tag{39}$$

The bound states in the QWs of the device have been taken into consideration in the present analysis by using a self-consistent quantum drift-diffusion (SCQDD) model (Acharyya and Ghosh, 2017; Ghosh et al., 2017). The said model consists of fundamental classical drift-diffusion (CLDD) equations coupled with Schrödinger equations associated with both conduction and valence bands of the device structure under reverse bias. The CLDD equations are given by:

$$\frac{\partial}{\partial x}\left(\varepsilon(x)\frac{\partial^{(j)}V(\lambda, x)}{\partial x}\right) = q\begin{Bmatrix}\left({}^{(j)}\gamma_p(\lambda, x)\,{}^{(j)}p_p(\lambda, x)\right)\\ -\left({}^{(j)}\gamma_n(\lambda, x)\,{}^{(j)}n_n(\lambda, x)\right) + N(x)\Big|_{ITXS}\end{Bmatrix} \tag{40}$$

$$\frac{\partial^{(j)}J_r^{(total)}(\lambda, x)}{\partial x} = \pm q\begin{pmatrix}{}^{(j)}G_r^{(AV)}(\lambda, x) + {}^{(j)}G_r^{(BBT)}(\lambda, x)\\ +{}^{(j)}G_r^{(TAT)}(\lambda, x) - {}^{(j)}R_r(\lambda, x)\end{pmatrix} \tag{41, 42}$$

$${}^{(j)}J_r^{(total)}(\lambda, x) = -q\begin{Bmatrix}\left({}^{(j)}\gamma_r(\lambda, x)\,{}^{(j)}r_r(\lambda, x)\right)\mu_r(x)\dfrac{\partial^{(j)}V(\lambda, x)}{\partial x}\\ \pm D_r(x)\dfrac{\partial\left({}^{(j)}\gamma_r(\lambda, x)\,{}^{(j)}r_r(\lambda, x)\right)}{\partial x}\end{Bmatrix} + J_{r(opt)}^{(total)}(\lambda)\Big|_{ITXS} \tag{43, 44}$$

where ${}^{(j)}V(\lambda, x)$, ${}^{(j)}p_p(\lambda, x)$, ${}^{(j)}n_n(\lambda, x)$, ${}^{(j)}J_p^{(total)}(\lambda, x)$ and ${}^{(j)}J_n^{(total)}(\lambda, x)$ are electric potential, hole and electron densities and hole and electron current densities respectively at j^{th} iteration. All of these said parameters are functions of both the space coordinates 'x' and the wavelength of optical illumination 'λ'. The parameters $\mu_r(x)$, $D_r(x)$ and $\varepsilon(x)$ are space dependent mobility, diffusivity and permittivity. The space dependent material parameters can be represented in the following form:

$$\left.\begin{aligned}\Xi(x) &= \Xi^{(Si)} && \Omega^{(Si)}\\ &= \Xi^{(3C-SiC)} && \Omega^{(3C-SiC)}\end{aligned}\right\} \tag{45}$$

where $\Xi^{(Si)}$ is the value of that parameter in a region made of *Si* ($\Omega^{(Si)}$) and $\Xi^{(3C-SiC)}$ is the value of that parameter in a region made of 3C-SiC ($\Omega^{(3C-SiC)}$). The parameters ${}^{(j)}\gamma_r(\lambda, x)$ are the quantum correction factors associated with hole or electron concentration at j^{th} iteration. At the first iteration, i.e., j = 1, the values of the quantum correction factor are initiated as unity at all space points (${}^{(1)}\gamma_r(\lambda, x) = 1$). The field dependent expressions of avalanche generation rate ($G_r^{(AV)}(\lambda, x)$), band-to-band tunnelling generation rate ($G_r^{(BBT)}(\lambda, x)$), trap assisted tunnelling generation rate ($G_r^{(TAT)}(\lambda, x)$) and Shockley-Read-Hall recombination rate ($R_r(\lambda, x)$) of the charge carriers have already been mentioned in the earlier report by the authors (Acharyya and Ghosh, 2017; Ghosh et al., 2017).

The DD equations given in equations (1)–(5) can be solved simultaneously at any iteration 'j', subject to appropriate boundary conditions imposed on electric potential, gradient of electric potential (i.e., electric field ${}^{(j)}\xi(\lambda, x) = -\partial^{(j)}V(\lambda, x) / \partial x$) and current densities at the edges of the π-layer for either ITNS or ITPS configurations. Those are given by:

$$\left.\begin{aligned} {}^{(j)}V(\lambda, x=0)\big|_{ITNS} &= +V_R, \quad {}^{(j)}V\left(\lambda, x=W_i\right)\big|_{ITNS} = 0 \\ {}^{(j)}V(\lambda, x=0)\big|_{ITPS} &= 0, \quad {}^{(j)}V\left(\lambda, x=W_i\right)\big|_{ITPS} = +V_R \end{aligned}\right\} \tag{46, 47}$$

$$\left.\frac{\partial\, {}^{(j)}V(\lambda, x)\big|_{ITXS}}{\partial x}\right|_{x=0} = \left.\frac{\partial\, {}^{(j)}V(\lambda, x)\big|_{ITXS}}{\partial x}\right|_{x=W_i} = 0 \tag{48, 49}$$

$$\left.\begin{aligned} {}^{(j)}NJ(\lambda, x=0)\big|_{ITNS} &= \left(\frac{2\,{}^{(j)}J_p^{(total)}(\lambda, x=0)\big|_{ITNS}}{{}^{(j)}J_p^{(total)}(\lambda, x=0)\big|_{ITNS} + {}^{(j)}J_n^{(total)}(\lambda, x=0)\big|_{ITNS}} - 1\right) \\ {}^{(j)}NJ\left(\lambda, x=W_i\right)\big|_{ITNS} &= \left(1 - \frac{2\,{}^{(j)}J_n^{(total)}\left(\lambda, x=W_i\right)\big|_{ITNS}}{{}^{(j)}J_p^{(total)}\left(\lambda, x=W_i\right)\big|_{ITNS} + {}^{(j)}J_n^{(total)}\left(\lambda, x=W_i\right)\big|_{ITNS}}\right) \end{aligned}\right\} \tag{50, 51}$$

$$\left.\begin{aligned} {}^{(j)}NJ(\lambda, x=0)\big|_{ITPS} &= \left(1 - \frac{2\,{}^{(j)}J_n^{(total)}(\lambda, x=0)\big|_{ITPS}}{{}^{(j)}J_p^{(total)}(\lambda, x=0)\big|_{ITPS} + {}^{(j)}J_n^{(total)}(\lambda, x=0)\big|_{ITPS}}\right) \\ {}^{(j)}NJ(\lambda, x=W_i)\big|_{ITPS} &= \left(\frac{2\,{}^{(j)}J_p^{(total)}\left(\lambda, x=W_i\right)\big|_{ITPS}}{{}^{(j)}J_p^{(total)}\left(\lambda, x=W_i\right)\big|_{ITPS} + {}^{(j)}J_n^{(total)}\left(\lambda, x=W_i\right)\big|_{ITPS}} - 1\right) \end{aligned}\right\} \tag{52, 53}$$

where ${}^{(j)}NJ(\lambda, x)|_{ITXS}$ is the normalised current density parameter given by:

$${}^{(j)}NJ(\lambda, x)\big|_{ITXS} = \left(\frac{{}^{(j)}J_p^{(total)}(\lambda, x)\big|_{ITXS} - {}^{(j)}J_n^{(total)}(\lambda, x)\big|_{ITXS}}{{}^{(j)}J_p^{(total)}(\lambda, x)\big|_{ITXS} + {}^{(j)}J_n^{(total)}(\lambda, x)\big|_{ITXS}}\right) \tag{54}$$

The simultaneous numerical solution of the CLDD equations (40)–(44) subject to the boundary conditions given in equations (46)–(53) due to either ITNS or ITPS provide the special variations of ${}^{(j)}V(\lambda, x)$, ${}^{(j)}p_p(\lambda, x)$, ${}^{(j)}n_n(\lambda, x)$, ${}^{(j)}J_p^{(total)}(\lambda, x)$ and ${}^{(j)}J_n^{(total)}(\lambda, x)$ at j^{th} iteration. But these parameters have been obtained without taking into account the bound states within the QWs. The consideration of those bound states can be introduced

in the solutions by solving the 1D time-independent Schrödinger equations corresponding to valence band and conduction band respectively. Those are given by:

$$-\frac{\partial}{\partial x}\hat{x}.\left(\frac{\hbar^2}{2m_p^*(x)}\frac{\partial {}^{(j)}\psi_p^{Z_p}(\lambda,x)}{\partial x}\hat{x}\right) + {}^{(j)}E_v(\lambda,x)\,{}^{(j)}\psi_p^{Z_p}(\lambda,x) = {}^{(j)}E_p^{Z_p}(\lambda)\,{}^{(j)}\psi_p^{Z_p}(\lambda,x) \tag{55}$$

$$-\frac{\partial}{\partial x}\hat{x}.\left(\frac{\hbar^2}{2m_n^*(x)}\frac{\partial {}^{(j)}\psi_n^{Z_n}(\lambda,x)}{\partial x}\hat{x}\right) + {}^{(j)}E_c(\lambda,x)\,{}^{(j)}\psi_n^{Z_n}(\lambda,x) = {}^{(j)}E_n^{Z_n}(\lambda)\,{}^{(j)}\psi_n^{Z_n}(\lambda,x) \tag{56}$$

where $m_{p,n}^*(x)$ are the spatially varying effective mass of holes in valence band and electrons in conduction band [using *k.p* method the effective mass of holes takes into account the three separate bands having doubly degeneracy as a result of the spin away from $k = 0$ in valence band (Acharyya and Ghosh, 2017; Costato and Reggiani, 1970)], ${}^{(j)}\psi_r^{Z_r}(\lambda,x)$ and ${}^{(j)}E_r^{Z_r}(\lambda)$ are the wave function solutions and eigen-energy states corresponding to the valence band ($r \equiv p$) and conduction band ($r \equiv n$). The superscripts z_p and z_n denote the number of modes (typically $z_r = 5 - 10$) corresponding to the solution associated with valence band and conduction band respectively, $\hbar = h / 2\pi$ is the normalised Plank's constant. At the j^{th} iteration, the energy states associated with the edges of the conduction band (${}^{(j)}E_c(\lambda,x)$) and the valence band (${}^{(j)}E_v(\lambda,x)$) can be obtained from the electric potential solution ${}^{(j)}V(\lambda,x)$ obtained earlier in the same iteration and from the knowledge of the spatially varying energy-bandgap obtained in the earlier iteration ($\{{}^{(j-1)}E_g(\lambda,x)$ for $j>1\}$, $\{{}^{(1)}E_g(x) = E_g^{(Si)}$ at $\Omega^{(Si)}$, ${}^{(1)}E_g(x) = E_g^{(3C-SiC)}$ at $\Omega^{(3C-SiC)}$ for $j=1\}$). Those relations are given by (Acharyya and Ghosh, 2017):

$${}^{(j)}E_c(\lambda,x) = -q\,{}^{(j)}V(\lambda,x) + \frac{1}{2}\left[{}^{(j-1)}E_g(\lambda,x) + k_BT\ln\left(\frac{N_c(x)}{N_v(x)}\right)\right] \tag{57}$$

$${}^{(j)}E_v(\lambda,x) = {}^{(j)}E_c(\lambda,x) - {}^{(j-1)}E_g(\lambda,x) \tag{58}$$

where $k_B = 1.38 \times 10^{-23}$ J K^{-1} is the Boltzmann constant, T is the absolute temperature in Kelvin (K), $N_c(x)$ and $N_v(x)$ are the spatially varying effective density of states in conduction and valence bands respectively. The equations (57) and (58) are derived from carrier concentration equations ${}^{(j)}n_n(\lambda,x) = N_c(x)exp\{-({}^{(j)}q\varphi_n(\lambda,x) + {}^{(j)}E_c(\lambda,x)) / k_BT\} = n_i(x)exp\{q({}^{(j)}V(\lambda,x) - {}^{(j)}\varphi_n(\lambda,x)) / k_BT\}$ and ${}^{(j)}p_p(\lambda,x) = N_v(x)exp\{({}^{(j)}q\varphi_p(\lambda,x) + {}^{(j)}E_v(\lambda,x)) / k_BT\} = n_i(x)exp\{q({}^{(j)}\varphi_p(\lambda,x) - {}^{(j)}V(\lambda,x)) / k_BT\}$ under no-equilibrium condition and from the relation ${}^{(j)}E_v(\lambda,x) = {}^{(j)}E_c(\lambda,x) - {}^{(j-1)}E_g(\lambda,x)$; where ${}^{(j)}\varphi_n(\lambda,x)$ and ${}^{(j)}\varphi_p(\lambda,x)$ are quasi-Fermi potentials associated with respective charge carriers (Selberherr, 1984). After solving the Schrödinger's equations at j^{th} iteration for the given heterostructure, z_r sets of wave function solutions (${}^{(j)}\psi_r^{Z_r}(\lambda,x)$) as well as z_r sets of eigen-energy states (${}^{(j)}E_r^{Z_r}(\lambda)$) can be obtained. Now, the quantum electron and hole densities can be calculated as:

$$^{(j)}n_n^{(qunt)}(\lambda, x) = \sum_{Z_n}\left({}^{(j)}N_n^{Z_n}(\lambda)\left|{}^{(j)}\psi_n^{Z_n}(\lambda, x)\right|^2\right) \tag{59}$$

$$^{(j)}p_p^{(qunt)}(\lambda, x) = \sum_{Z_p}\left({}^{(j)}N_p^{Z_p}(\lambda)\left|{}^{(j)}\psi_p^{Z_p}(\lambda, x)\right|^2\right) \tag{60}$$

where $^{(j)}N_n^{Z_n}(\lambda)$ is the sub-band electron occupation density in conduction band and $^{(j)}N_p^{Z_p}(\lambda)$ is the sub-band hole occupation density in valence band at j^{th} iteration. Those are:

$$^{(j)}N_n^{Z_n}(\lambda) = \int_{^{(j)}E_n^{Z_n}(\lambda)}^{\infty} g_c(E)\,{}^{(j)}f_{FDn}(\lambda, E)dE \tag{61}$$

$$^{(j)}N_p^{Z_p}(\lambda) = \int_{-\infty}^{^{(j)}E_p^{Z_p}(\lambda)} g_v(E)\,{}^{(j)}f_{FDp}(\lambda, E)dE \tag{62}$$

where $g_c(E) = (m_n^*/\pi\hbar^2)$ and $g_v(E) = (m_p^*/\pi\hbar^2)$ are the 2D density of states functions in conduction band and valance band respectively within the QWs (Weisbuch and Vinter, 1991), the distribution functions $^{(j)}f_{FDn}(\lambda, E)$ and $^{(j)}f_{FDp}(\lambda, E)$ are the Fermi-Dirac distribution functions associated with respective charge carriers which are $^{(j)}f_{FDn}(\lambda, E) = 1\Big/\left(1+\exp\left(\left(E - {}^{(j)}E_{Fn}(\lambda)\right)\Big/k_BT\right)\right)$ and $^{(j)}f_{FDp}(\lambda, E) = 1\Big/\left(1+\exp\left(\left({}^{(j)}E_{Fp}(\lambda) - E\right)\Big/k_BT\right)\right)$ respectively at j^{th} iteration, $^{(j)}E_{Fn}(\lambda)$ and $^{(j)}E_{Fp}(\lambda)$ are the quasi-Fermi energy levels corresponding to the respective charge carriers under non-equilibrium condition at j^{th} iteration. Under non-equilibrium condition, the magnitude of $|^{(j)}E_{Fn}(\lambda) - {}^{(j)}E_{Fp}(\lambda)|$ quantifies how far extent the semiconductor material is removed from its equilibrium; under non-equilibrium condition the relationship between electron and hole densities is $^{(j)}n_n(\lambda, x)\,{}^{(j)}p_p(\lambda, x) = n_i^2(x)\exp(^{(j)}E_{Fn}(\lambda) - {}^{(j)}E_{Fp}(\lambda)\big/k_BT)$. Now the space dependent quantum correction factors can be defined corresponding to both electron and hole densities obtained at the end of j^{th} iteration. Those are given by:

$$\begin{aligned} ^{(j)}\gamma_r(\lambda, x) &= \left(\frac{^{(j)}r_r^{(qunt)}(\lambda, x)}{^{(j)}r_r(\lambda, x)}\right) \qquad \Omega_{QW} \\ &= 1 \qquad\qquad\qquad\quad Otherwise \end{aligned} \tag{63}$$

At the starting of the next iteration $(j + 1)$ for $j \geq 2$, the refined or quantum-corrected electron and hole densities have been incorporated in the equations (40)–(44) and the entire procedure is repeated until the deviations of $^{(j)}V(\lambda, x)$, $^{(j)}p_p(\lambda, x)$, $^{(j)}n_n(\lambda, x)$, $^{(j)}J_p^{(total)}(\lambda, x)$ and $^{(j)}J_n^{(total)}(\lambda, x)$ in the present iteration (j^{th}) with respect to the earlier iteration ($(j-1)^{\text{th}}$) becomes smaller than the pre-specified values. The said inter-iteration deviations can be obtained from:

$$^{(j)}\Delta_{\aleph}(\lambda) = \left[\sum_{x} \frac{^{(j)}\aleph(\lambda, x) - {}^{(j-1)}\aleph(\lambda, x)}{\left(\sum_{x} {}^{(j)}\aleph(\lambda, x) \right)} \right] \tag{64}$$

where $^{(j)}\aleph(\lambda, x) \equiv {}^{(j)}V(\lambda, x), {}^{(j)}p_p(\lambda, x), {}^{(j)}n_n(\lambda, x), {}^{(j)}J_p^{(total)}(\lambda, x), {}^{(j)}J_n^{(total)}(\lambda, x)$. If all the deviations are found to be $^{(j)}\Delta_{\aleph}(\lambda) \leq 10^{-3}$, then the self-consistent solutions are assumed to be achieved, and the iterations are stopped. Afterward, the self-consistent solutions of the parameters $V_{(SC)}(\lambda, x)$, $p_{p(SC)}(\lambda, x)$, $n_{n(SC)}(\lambda, x)$, $J_{p(SC)}^{(total)}(\lambda, x)$ and $J_{n(SC)}^{(total)}(\lambda, x)$ are assumed to be obtained. The details of the algorithm for obtaining the self-consistent solution of electric potential, electric field and carrier densities as functions of space points have been already discussed by authors earlier (Acharyya and Ghosh, 2017; Ghosh et al., 2017). The Poisson's equation and the Schrödinger's equations have been numerically solved by using 1D finite difference method (FDM) (Doudlas and Yuan, 1987) and forth order Runge-Kutta (RK4) method (Christodoulou, 2009) respectively. The mixing algorithm proposed by Stern (1970) has also been used to ensure the convergence of the abovementioned algorithm.

Once the self-consistent solutions are obtained, the total terminal current for a given reverse bias of VR can separately be obtained for ITNS and ITPS configurations. Those are given by:

$$\left.\begin{aligned} J_{(SC)}^{(total)}(\lambda)\Big|_{ITNS} &= \left(\frac{1}{W_n + W_i + W_p} \right) \int_{x=-W_n}^{x=W_i+W_p} \left(\begin{matrix} J_{n(SC)}^{(total)}(\lambda, x)\Big|_{ITNS} \\ + J_{p(SC)}^{(total)}(\lambda, x)\Big|_{ITNS} \end{matrix} \right) dx \\ J_{(SC)}^{(total)}(\lambda)\Big|_{ITPS} &= \left(\frac{1}{W_n + W_i + W_p} \right) \int_{x=-W_p}^{x=W_i+W_n} \left(\begin{matrix} J_{n(SC)}^{(total)}(\lambda, x)\Big|_{ITPS} \\ + J_{p(SC)}^{(total)}(\lambda, x)\Big|_{ITPS} \end{matrix} \right) dx \end{aligned}\right\} \tag{65, 66}$$

The dark current as a function of V_R can be obtained from either equations (65) or (66) after getting the self-consistent solution for input optical power of $P_{opt} = 0$, i.e.:

$$J_{(SC)}^{(dark)} = \left(J_{(SC)}^{(total)}(\lambda)\Big|_{ITNS} \right)\Big|_{P_{opt}=0} = \left(J_{(SC)}^{(total)}(\lambda)\Big|_{ITPS} \right)\Big|_{P_{opt}=0} \tag{67}$$

Once the dark current is obtained for a given reverse bias voltage of V_R, the total photocurrent for either ITNS or ITPS configuration can be obtained from the following equation, after recalculating the self-consistent solutions for a given P_{opt} of a given wavelength λ, i.e.:

$$J_{(SC)}^{(opt)}(\lambda)\Big|_{ITXS} = \left(J_{(SC)}^{(total)}(\lambda)\Big|_{ITXS} - J_{(SC)}^{(dark)} \right) \tag{68}$$

Now, the optical gain for a given set of V_R, P_{opt} and λ, can be obtained as:

$$M_{(opt)}(\lambda)\big|_{ITXS} = \left(\frac{J_{(SC)}^{(opt)}(\lambda)\big|_{ITXS}}{J_{(opt)}^{(total)}(\lambda)\big|_{ITXS}} \right) \tag{69}$$

Finally, the un-multiplied as well as the multiplied responsivities for a given set of V_R, P_{opt} and λ, can be obtained from the following equations:

$$\left.\begin{aligned} \Re^{UM}(\lambda)\big|_{ITXS} &= \left(\frac{A_j\, J_{(opt)}^{(total)}(\lambda)\big|_{ITXS}}{P_{opt}} \right) \\ \Re^{M}(\lambda)\big|_{ITXS} &= M_{(opt)}(\lambda)\big|_{ITXS} \left(\frac{A_j\, J_{(opt)}^{(total)}(\lambda)\big|_{ITXS}}{P_{opt}} \right) \end{aligned}\right\} \tag{70, 71}$$

The theoretical model presented in the earlier section has been used to simulate the current-voltage (I-V), optical gain and spectral response characteristics of MQB nano-APDs based on Si~3C-SiC material system; the simulation results have been presented in this section. The material parameters of Si and 3C-SiC at 300 K, used in the present simulation have been taken from the published reports (Rajkanan et al., 1979; Spitzer and Fan, 1957; Hara and Nishi, 1966; Solangi and Chaudry, 1992; Mukherjee and Das, 2014; Manasreh, 2005; Grant, 1973; Bellotti et al., 1999; Mickevicius and Zhao, 1998; Canali et al., 1971; IOFFE, 2019; Zeghbroeck, 2011; May, 2005; Yan-Kun et al., 2012). The I-V characteristics of the nano-APDs have been obtained from the simulation for the dark condition as well as for two different illumination configurations, i.e., ITNS and ITPS by varying the number of QBs from zero (N_b = 0) to five (N_b = 5). It was reported earlier that the breakdown voltage (V_B) of the structures under consideration, varies from 9.13 to 9.39 V (Acharyya and Ghosh, 2017) as the number of QBs varies from zero (N_b = 0) to five (N_b = 5). Thus the applied bias voltage should be just below the breakdown voltage in order to achieve high optical gain without significant increase in the dark current; the applied reverse bias may be chosen to be V_R = 9 V < V_B. The I-V characteristics of:

a Si flat nano APD

b MQB nano-APD having N_b = 5, under both dark condition and ITPS configuration have been shown in Figures 3(a) and 3(b) respectively for the incident optical power (P_{opt}) of 0, 10, 100, 500 and 1,000 mW ($\Phi_0(\lambda)$ = 0, 0.71×10^{30}, 7.12×10^{30}, 30.56×10^{30} and 71.21×10^{30} m^{-2} s^{-1}) of λ = 850 nm wavelength.

It is observed from the Figures 3(a) and 3(b) that the dark current of the device reduces from 0.40 to 0.24 nA due to the increase number of QBs from 0 to 5; whereas the photocurrent due to ITPS is also found to be decreasing significantly due to the introduction of QBs.

In order to clearly understand the effect of QBs on the photocurrent, the current versus N_b plots are shown in Figure 4. Figure 4 shows current versus N_b plots for dark condition (P_{opt} = 0 mW) as well as both ITNS and ITPS configurations for different optical power (P_{opt} = 10, 100, 500 and 1,000 mW, i.e., $\Phi_0(\lambda)$ = 0, 0.71×10^{30}, 7.12×10^{30}, 30.56×10^{30} and 71.21×10^{30} m^{-2} s^{-1}) of 850 nm wavelength.

Figure 3 The I-V characteristics of, (a) Si flat nano-APD (b) MQB nano-APD having $N_b = 5$, under dark condition and for ITPS configuration, for different incident optical powers of 850 nm wavelength

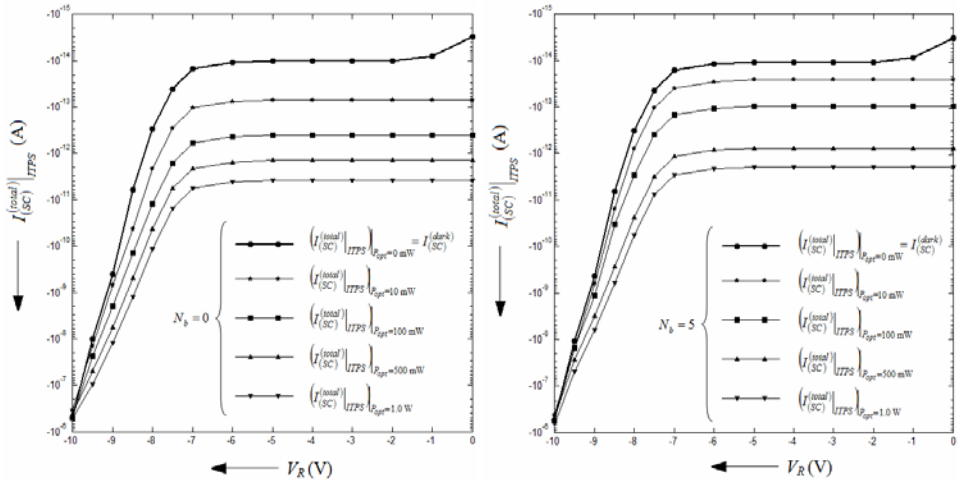

(a) (b)

Figure 4 Variations of total current in nano-APDs for the reverse bias voltage of 9.0 V with the number of QBs, under dark condition and both types of illumination configurations such as ITNS and ITPS for different incident optical powers of 850 nm wavelength

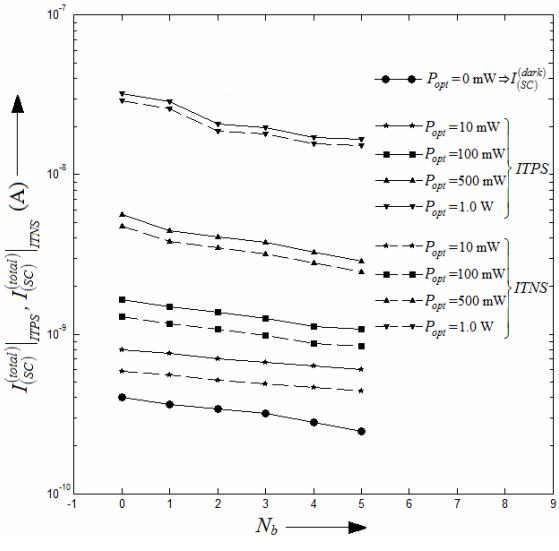

It is observed from Figure 4 that the value of photocurrent is always greater in ITPS configuration than the ITNS configuration for all values of N_b. For example, the photocurrent under ITPS configuration rises from 0.24 to 16.76 nA at the reverse bias of 9 V due to the increment of incident optical power (P_{opt}) of wavelength 850 nm from 0 to 1.0 W (i.e., $\Phi_0(\lambda) = 0 - 71.21 \times 10^{30}$ m^{-2} s^{-1}) in MQB nano-APD having $N_b = 5$;

the same increment is found to be 0.40 to 32.10 nA in Si flat nano-APD. However, the photocurrent increments in ITNS configuration are found to be 0.24–15.25 nA and 0.40–29.80 nA respectively. The greater photocurrents in ITPS configuration as compared to those in ITNS configuration can be explained as follows. When the light is illuminated on p^+-layer (ITPS), then the photo-generated electrons in p^+-layer enter to the π-layer and get multiplied by avalanche multiplication phenomena; whereas the photo generated holes in p^+-layer come out of the device without getting the opportunity to be multiplied. Therefore, the photocurrent in ITPS configuration is primarily electron dominated. On the reverse way, the photocurrent in ITNS configuration is primarily hole dominated. Now, in Si, the ionisation rate of electrons is significantly greater than that of holes $(\zeta_n^{(Si)} > \zeta_p^{(Si)})$ for all electric field values at 300 K (Grant, 1973). Consequently, the electron dominated photocurrent in ITPS configuration gets greater amount of multiplication or optical gain as compared to the hole dominated photocurrent in ITNS configuration. This is the reason behind the greater multiplied photocurrent in ITPS configuration as compared to its ITNS counterpart. However, with the increase of number of QBs, the amounts of 3C-SiC material increases within the avalanche zone of the device near the n^+-π junction. Moreover, in 3C-SiC, the ionisation rate of electrons are smaller than that of holes $(\zeta_n^{(3C-SiC)} < \zeta_p^{(3C-SiC)})$ for all electric field values at 300 K (Bellotti et al., 1999; Mickevicius and Zhao, 1998). Thus the greater contribution of 3C-SiC material, in the APDs having higher N_b value, reduces the difference between the photocurrents in ITPS and ITNS configurations. That is way, the difference between the photocurrents ITPS and ITNS configurations are found to be 2.30 nA in Si flat nano-APD; while the same difference is only 1.51 nA in MQB nano-APD having $N_b = 5$.

Figure 5 Variations of optical gain of MQB nano-APDs with reverse bias voltage for different number of QBs, under dark condition and both types of illumination configurations such as, (a) ITNS (b) ITPS for the incident optical power of 1.0 W of 850 nm wavelength (see online version for colours)

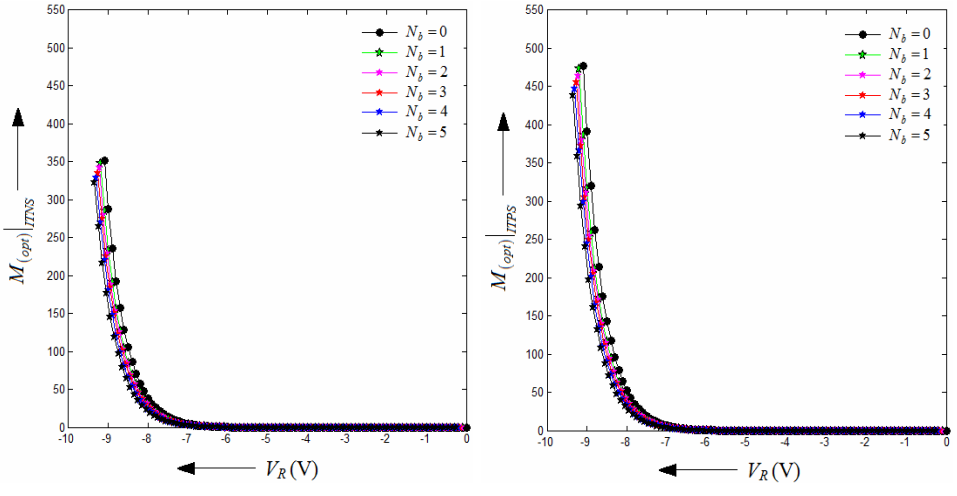

The variations of optical gain of MQB nano-ADPs with reverse bias for different N_b values are shown in Figures 5(a) and 5(b) for the dark condition and both ITNS and ITPS configurations for the incident optical power of P_{opt} = 1.0 W [i.e., $\Phi_0(\lambda) = 71.21 \times 10^{30}$ m^{-2} s^{-1}] of 850 nm wavelength. Obviously, the optical gain of the device is found to be significant greater in case of ITPS configuration than the ITNS configuration; the reason behind it has already been discussed in the earlier paragraph. It is notable from the Figures 5(a) and 5(b) that the optical gain decreases slightly due to the increase of N_b.

The most significant characteristic of an optical receiver is the operating wavelength. The choice of the most appropriate APD for a given optical communication system initiates by selecting the APD, which will provide the maximum responsivity at the operating wavelength of the system. The spectral response of a nano-APD primarily depends on the thickness of the absorption region (here π-region), appropriate anti-reflection coating on the incidence side of the photon flux (here either n^+- or p^+-side), the effective thickness of the front contact layer (here either W_n or W_p) as well as the biasing condition. The absorption coefficient of the base material system and the structural profile of the absorption layer (i.e., either flat or MQB structure) are the most important factors which determine the spectral response of the device. The spectral responses of nano-APDs having different number of QBs (N_b = 0, 1, 2, 3, 4 and 5) at the reverse bias of 9 V have been shown in Figures 6(a) and 6(b); the spectral responses have been obtained for the incident optical power of 1.0 W within the wavelength range of 200–4,000 nm under both ITNS and ITPS configurations. It is observed from Figures 6(a) and 6(b) that the peak responsivity for both INTS and ITPS configurations are obtained at the wavelength of 850 nm; the value of peak responsivities are 58.3 and 79.5 A W^{-1} respectively. The peak responsivity of the device decreases with the increase of the number of QBs due to the decrement of optical gain as mentioned earlier. The ITPS configuration provides better spectral response than the ITNS configuration as a result of the better avalanche multiplication attained by electron dominated photocurrent in ITPS and compared to the hole dominated photocurrent in ITNS. Thus the ITPS configuration is always preferable over ITNS configuration for the proposed structure under consideration. The optical absorption within the wavelength range of 400–1,100 nm is primarily due to interband absorption in Si. However, in MQB nano-APDs, the interband absorption in 3C-SiC layers causes slight increase in responsivity within the wavelength rage of 200–400 nm; responsivity within this range increases with the increase of number of QBs made of 3C-SiC. Now, the most noteworthy and important portion of the spectral response characteristics of the MQB nano-APDs is the intersubband absorptions in Si QWs beyond the wavelength of 1,100 nm. This intersubband absorption causes significant rise in responsivity within the wavelength range of 1,100–4,000 nm (short-wavelength infrared and mid-infrared wavelengths) when $N_b \geq 2$, i.e., $N_w \geq 1$. The peak responsivity at this longer wavelength range is observed to be 17.67 and 24.10 A W^{-1} in ITNS and ITPS configurations respectively at the wavelength of 2,600 nm. Responsivity peak associated with the longer wavelengths (i.e., 1,100–4,000 nm) at 2,600 nm wavelength is observed to be increase with the increase of the number of QWs from N_w = 1 to N_w = 4. Therefore, the proposed MQB nano-APD structure has the immense potential of detecting longer wavelengths almost up to 4,000 nm and its bandwidth is found to be significantly wider as compared to the Si flat nano-APDs.

Figure 6 Variations of spectral responsivity of MQB nano-APDs for the reverse bias of 9 V, with wavelength of incident optical power of 1.0 W for different number of QBs, under both types of illumination configurations such as, (a) ITNS (b) ITPS (see online version for colours)

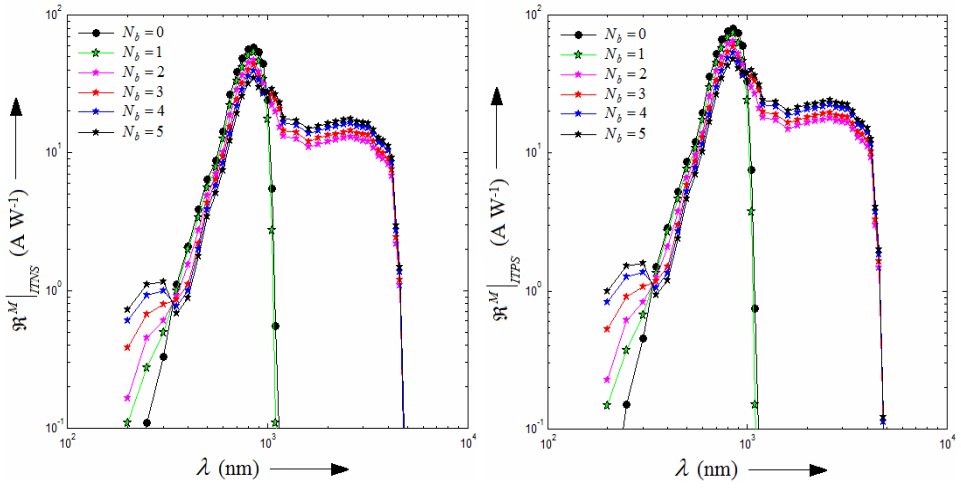

The PerkinElmer's (2018) C30902EH infrared APDs based on Si, fabricated with a double diffused 'reach-through' structure, provides high responsivity between 400–1,000 nm wavelengths. The peak responsivity of this APD is around 70–77 A W^{-1} at 830 nm wavelength. Also, the dark current range of C30902EH is 15–30 nA at the normal operating condition just below the breakdown voltage. However, the MQW nano-APD structure proposed in this paper is capable of providing the responsivity of almost 80 A W^{-1} (in ITPS configuration) with much smaller dark current (0.24–0.40 nA). The dark current of MQB nano-APD is found to be significantly smaller as compared to the n^+-p-π-p^+ structured Si flat APD reported by Wêgrzecka et al. (2004) in 2004. Furthermore, the capability of longer wavelength detection (up to 4,000 nm) of the proposed MQB nano-APDs makes those extremely versatile candidates for the potential applications in deep space astronomical observations.

It is more convenient to fabricate the MQB APD structures based on Si/3C-SiC/Si heterojunctions via liquid phase chemical vapour deposition (LPCVD) technique (Qamar et al., 2014) rather than the MBE growth technique (Arthur, 2002). The sub-10 nm thick single crystalline 3C-SiC barriers can be grown on Si (100) wells ($N_i = 10^{21}$ m^{-3}) by using a hot-wall LPCVD reactor at 1,000°C (Qamar et al., 2014). The trimethyaluminium (TMAl) can be used as the source of Al dopants (acceptors) in the in-situ doping process (Qamar et al., 2014). After the growth of the Si/3C-SiC/Si heterostructures, high temperature annealing steps (1,100°–1,300°C) are required in order to eliminate certain crystal defects and film stress due to inherent problems of lattice mismatch (~20%) and different thermal expansion coefficients (~20% at 1,200°C) between Si and 3C-SiC (Tanner et al., 2017). Conventional lithography processes may be used to create mesa test structures before plasma etching by using HCl and/or SF_6 in a STS ICP or a LAM 480 system. The metal contact from un-illuminated n^+ or p^+-layer may be deposited via sputter deposition of Cr (20 nm)/Au (100 nm) layers. A controlled optical window can be

realised on n^+-layer for ITNS or p^+-layer for ITPS via special sputter deposition of Cr (20 nm)/Au (100 nm) layers which was described elsewhere (Vyas et al., 1979, 1977; Schweighart et al., 1978). The Continuous Wave (CW) Tunable Ti:Sapphire Laser 3900S (2018) can be used as the wideband optical source for performing the experiments in order to obtain the spectral response of the MQB APDs.

4 Excess noise

The essential requirement for a low-noise APD is large difference between the ionisation rate of electrons and holes (Capasso et al., 1983). In 1966, McIntyre showed that low avalanche noise in APDs can be obtained when the ratio of ionisation rate of holes to electrons ($K_s^{(X)}$; where superscript 'X' stands for Si or 3C-SiC or Si~3C-SiC MQB) is either very large or very small. The parameter $K_s^{(X)}$ can be defined for Si or 3C-SiC or Si~3C-SiC MQB structure as:

$$K_s^{(X)} = \left(\frac{\zeta_p^{(X)}}{\zeta_n^{(X)}} \right) \tag{72}$$

where $\zeta_p^{(X)}$ and $\zeta_n^{(X)}$ are the ionisation rate of holes and electrons respectively in Si or 3C-SiC or Si~3C-SiC MQB structure; both of them are functions of electric field (ξ), which implies $K_s^{(X)}$ is a function of ξ. The variations of $K_s^{(Si)}$ and $K_s^{(3C-SiC)}$ with ξ have been shown in Figure 7(a) for the electric field range of 10^7–10^8 V m^{-1} which is the range of the electric field found to be present within the π-layer of the Si flat and Si~3C-SiC MQB APDs under consideration for the applied reverse bias of 9 V (Acharyya and Ghosh, 2017). However, the field variation within the multiplication region is found to be very small, nearly 3.36×10^7–3.58×10^7 V m^{-1} (Acharyya and Ghosh, 2017); within which both $K_s^{(Si)}$ and $K_s^{(3C-SiC)}$ are observed to have almost constant values of 0.32 and 1.48 respectively as shown in Figure 7(b). The field variations of ionisation rate of holes and electrons in Si and 3C-SiC have been taken from the empirical relations fitted from the experimentally measured or Monte Carlo simulated ionisation rate data (Grant, 1973; Bellotti et al., 1999; Mickevicius and Zhao, 1998). It is observed Figure 7(b) that $K_s^{(Si)}$ is not very much smaller than 1.0; thus $\zeta_p^{(Si)}$ and $\zeta_n^{(Si)}$ do not differ largely within the field range under consideration. Therefore, the multiplication noise in Si flat nano-APDs is inherently high.

However, the use of Si~3C-SiC MQB structure instead of the flat Si structure causes significant rise in the ratio of hole to electron ionisation rates. The impact ionisation rate depends exponentially on the ionisation threshold energy and on the energy from which the hole of electron starts to accelerate under applied electric field (Chin et al., 1980). It can be observed from the band structure of MQB nano-APD shown in Figure 2(a), the discontinuity in the valence band (ΔE_v = 0.99 eV) is significantly greater than that in the conduction band (ΔE_c = 0.25 eV) (Acharyya and Ghosh, 2017). This fact enhances the ionisation rates (Chin et al., 1980). In order to assess the effect of the band-edge step on the ionisation rate, consider a hole that travels from one 3C-SiC layer into a Si layer. When it arrives in the Si it 'observes' not only the smaller bandgap of the Si, but it also

starts at an energy ΔE_v (valence band edge step) below the Si band edge. Thus the energy ΔE_v has to be added with the ionisation threshold energy within a distance from the discontinuity equal to the impact ionisation mean free path. When this procedure is followed for electrons, the conduction band edge step ΔE_c is found to be much smaller. Therefore, $\zeta_p^{(MQB)}$ increases more than $\zeta_p^{(MQB)}$. Moreover, Holonyak and co-workers (Shichuo et al., 1978; Holonyak et al., 1980) showed that the phonon scattering rate for holes in MQW/MQB structures are more as compared to the bulk. Thus the mean free path of phonon scattering for holes is found to be less in MQB structure as compared to the bulk Si. This fact also affects the ratio of hole to electron ionisation rates (Chin et al., 1980; Shichuo et al., 1978; Holonyak et al., 1980). The parameter $K_s^{(MQB)}$ for different barrier numbers (N_b = 1 to 5) have been calculated as a function of electric field for the doping concentration of the active π-layer of $N_i = 10^{21}$ m^{-3} by following the method depicted by Chin et al. (1980); $K_s^{(MQB)}$ versus ξ plots for different N_b values have been shown in Figures 7(a) and 7(b). It is observed from Figure 7(b) that within the effective field range of 3.36×10^7–3.58×10^7 V m^{-1}, $K_s^{(MQB)}$ values remain almost constant and increases from 1.63 to 3.05 as N_b increases from 1 to 5. Therefore, increase of $K_s^{(MQB)}$ due to the use of MQB structure instead of bulk Si, the avalanche noise is expected to be lowered down (Capasso et al., 1983; Teich et al., 1996; Brennan and Haralson, 2000).

Figure 7 Variations of, (a) the ratio of hole to electron ionisation rate in Si flat, 3C-SiC flat and Si~3C-SiC MQB p^+-π-n^+ structures at 300 K with electric field within the depletion layer having doping density of 10^{21} m^{-3}(see online version for colours)

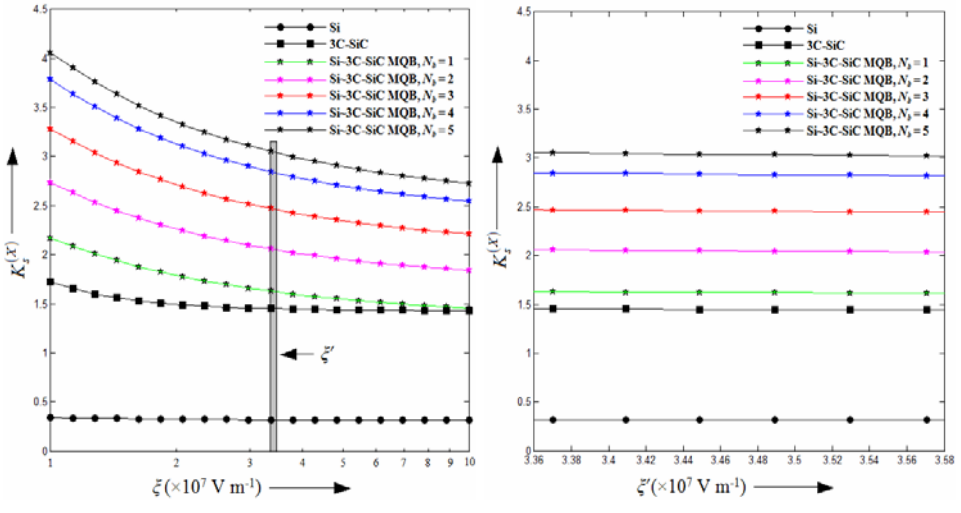

(a) (b)

Note: Figure 2(b) shows the above-mentioned variations within the operating field range of 3.36–3.58×10^7 V m^{-1} within the effective multiplication region.

4.1 Calculation of ENF in Si flat nano-APD

When the light energy is illuminated through p^+-side (ITPS) of the device, then only the photo-generated electrons in the p^+-region gets the opportunity to be multiplied, and the photocurrent is clearly electron dominated (Vyas et al., 1979). In this case, the multiplication gain can be obtained as follows. Initially the un-multiplied electron photocurrent density $(J_{n(opt)}^{(total)})$ containing both drift and diffusion components can be calculated as functions of wavelength (λ), incident optical power (P_{opt}) and applied reverse bias voltage (V_R) by following the procedure proposed by the authors. After that the spatial variation of the multiplied electron photocurrent density $(J_{n(SC)}^{(total)}(x))$ as functions of λ, P_{opt} and V_R can be obtained from the self-consistent solution of the coupled classical drift-diffusion (CLDD) and Schrödinger equations subject to appropriate boundary conditions imposed at the depletion layer edges. Thus, the multiplication factor will be the ratio of the multiplied electron photocurrent at $x = W_i$ to the injected un-multiplied electron photocurrent at $x = 0$. The multiplication factor/gain of Si flat nano-APD in ITPS configuration can be written as:

$$\langle M \rangle\Big|_{ITPS}^{(Si)} = \left(\frac{J_{n(SC)}^{(total)}(x = W_i)\Big|_{ITPS}}{J_{n(SC)}^{(total)}(x = 0)\Big|_{ITPS}} \right) \tag{73}$$

The ENF depends on the multiplication gain, on where the current is injected into the active π-layer and on the ratio of ionisation rates. For the constant value of $K_s^{(Si)}$ [Figure 2(b) shows it is constant throughout the effective field range) and electron-initiated multiplication process (in case of ITPS configuration], the ENF is given by (McIntyre, 1966; Brennan and Haralson, 2000):

$$F\Big|_{ITPS}^{(Si)} = \langle M \rangle\Big|_{ITPS}^{(Si)} \left\{ 1 - \left(1 - K_s^{(Si)}\right) \left(\frac{\langle M \rangle\Big|_{ITPS}^{(Si)} - 1}{\langle M \rangle\Big|_{ITPS}^{(Si)}} \right)^2 \right\} \tag{74}$$

4.2 Calculation of ENF in MQB nano-APDs

The expressions of average multiplication gain and ENF developed for supperlattice APDS by van Vliet et al. (1979) have been used in the present work for calculating those in MQB nano-APDs for different number of QBs. The average multiplication gain for the electron-initiated multiplication process (ITPS) is given by (van Vliet et al., 1979):

$$\langle M \rangle\Big|_{ITPS}^{(MQB)} = \left\{ \frac{(1+P)^m \left(1 - K_t^{(MQB)}\right)}{\left(1 + K_t^{(MQB)} P\right)^{m+1} - K_t^{(MQB)} (1+P)^{m+1}} \right\} \tag{75}$$

where m is the number of QB plus QW stages, P is the electron ionisation probability per stage, the parameter $K_t^{(MQB)}$ is given by:

$$K_t^{(MQB)} = \left(\frac{Q}{P}\right) \tag{76}$$

where Q is the hole ionisation probability per stage. The values of P and Q can be calculated from the following relations (Capasso et al., 1983):

$$P = \left\{\exp\left(\int_{z=0}^{z=(W_b+W_w)} \zeta_n^{(MQB)}(z)dz\right) - 1\right\} \tag{77}$$

$$Q = \left\{\exp\left(\int_{z=0}^{z=(W_b+W_w)} \zeta_p^{(MQB)}(z)dz\right) - 1\right\} \tag{78}$$

Now the ENF of a MQB nano-APD under ITPS configuration can be calculated from expression (van Vliet et al., 1979) given by:

$$F\big|_{ITPS}^{(MQB)} = 1 + \left\{\frac{\left[1 - \left(\frac{1}{\langle M\rangle\big|_{ITPS}^{(MQB)}}\right)\right]\left(1 - K_t^{(MQB)}\right)}{2 + P\left(1 + K_t^{(MQB)}\right)}\right\} \left\{2\left(\frac{1 - K_t^{(MQB)}P^2}{1 + K_t^{(MQB)}P}\right)\left[\langle M\rangle\big|_{ITPS}^{(MQB)} K_t^{(MQB)}\left(\frac{1+P}{1-K_t^{(MQB)}}\right) + \left(\frac{1}{1+P}\right)\right] - P\right\} \tag{79}$$

The excess noise characteristics of Si~3C-SiC MQB nano-APDs have been numerically calculated for different number of QBs and finally those are compared with the excess noise characteristics of Si flat nano-APD. The material parameters of Si and 3C-SiC at 300 K, used in the present simulation have been taken from the published reports (Rajkanan et al., 1979; Spitzer and Fan, 1957; Hara and Nishi, 1966; Solangi and Chaudry, 1992; Mukherjee and Das, 2014; Manasreh, 2005; Ghosh et al., 2017; Costato and Reggiani, 1970; Selberherr, 1984; Weisbuch and Vinter, 1991; Doudlas and Yuan, 1987; Christodoulou, 2009; Stern, 1970; Grant, 1973; Bellotti et al., 1999; Mickevicius and Zhao, 1998; Canali et al., 1971; IOFFE, 2019; Zeghbroeck, 2011; May, 2005; Yan-Kun et al., 2012). The ITPS configuration has been selected for the present study, since ITPS configuration of the devices under consideration provides better spectral response as compared to their ITNS counterparts. The excess noise theory of McIntyre (1966) rightly suggests the entire elimination of the secondary carrier multiplication leads to lowest noise operation of an APD. It has already been discussed in the earlier section that due to the larger valence band discontinuity than the conduction band discontinuity ($\Delta E_c < \Delta E_v$) in the energy-band structure of Si~3C-SiC MQB nano-APDs, the ratio of hole to electron ionisation rates ($K_s^{(MQB)}$) increases significantly with the increase of N_b. The value of the said ratio becomes significantly high ($K_s^{(MQB)} = 3.05$) for $N_b = 5$, which clearly indicates the suppression of electron multiplication in the conduction band and enhancement of hole multiplication in the valence band; and obviously hole ionisation rate is especially deterministic as discussed earlier.

The multiplication gain of the MQB nano-APDs have been plotted against the electron ionisation probability per stage in Figure 8 for different number of QBs ranging from 1 to 5. It is observed from Figure 8 that the rate of increase of the gain with respect to the electron impact ionisation probability per stage decreases with the increase of N_b. With the increase of N_b, the ionisation rate of holes in MQB structure rises, and also the hole ionisation becomes more spatially deterministic in nature, which leads to reduction in multiplication gain for a particular value of electron ionisation probability per stage.

Figure 8 Variations of gain of Si~3C-SiC MQB nano-APDs with the electron impact ionisation probability per stage for different number of stages (see online version for colours)

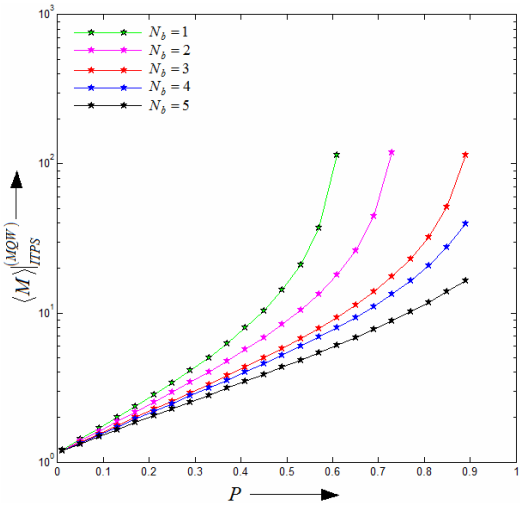

Figure 9 Variations of ENF of Si~3C-SiC MQB nano-APDs with the electron impact ionisation probability per stage for different number of stages (see online version for colours)

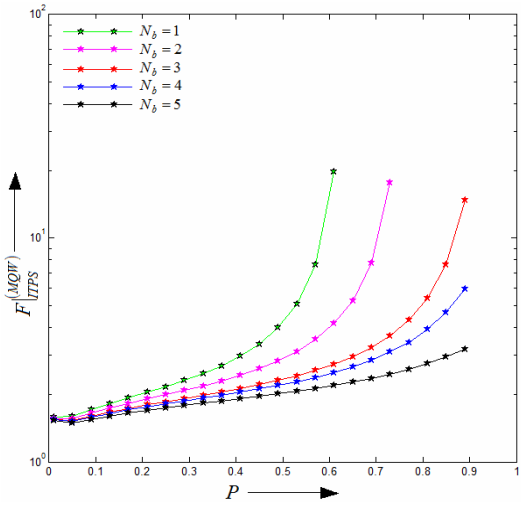

Figure 9 shows the variations of ENF of MQB nano-APDs with electron ionisation probability per stage for different N_b values ranging from 1 to 5. Figure 9 depicts the fact

that ENF of the device reduces rapidly for a particular value of electron ionisation probability per stage with the increase of N_b. It is clear that more spatially deterministic hole ionisation phenomena and enhanced hole ionisation rate at higher N_b values is the primary cause of reduction in multiplication gain and thereby decrease in ENF for a given value of electron ionisation probability per stage.

Finally, the variations of ENF of Si flat nano-APD and Si~3C-SiC MQB nano-APDs with multiplication gain have been shown in Figure 10. It is noteworthy from Figure 10 that the ENFs of the MQB APDs are significantly smaller than the Si flat nano-APD for given value of the multiplication gain. Suppression of electron ionisation is the primary cause of improvement of noise characteristics of MQB APDs as compared to their Si flat counterparts. However, it is notable from the Figure 10 that the increase in the number of QBs (N_b) restricts the maximum achievable gain of the MQB APDs. But the ENF versus gain plots become almost flat as the value of N_b increases, which approaches to practically noise free operation corresponding to $P \rightarrow 0$ and $Q \rightarrow \infty$, i.e., complete suppression of the secondary electron multiplication at low gain.

Figure 10 Variations of ENF of Si flat nano-APD and Si~3C-SiC MQB nano-APDs with gain (see online version for colours)

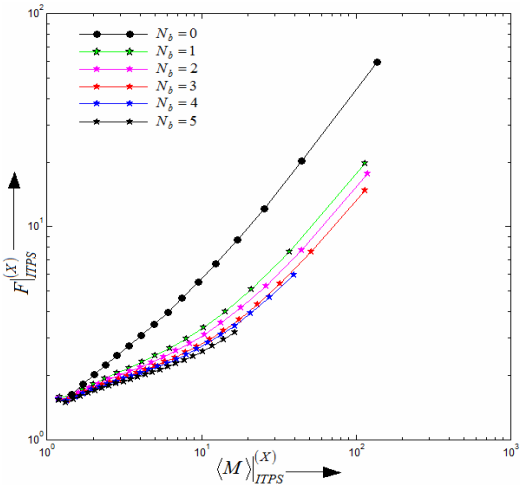

The experimentally measured ENF of commercially available Hamamatsu's short-wavelength type infrared Si APDs such as S5343, S5344 and S5345 remains within the range of 3.0–8.5 for the multiplication gain ranging from 5.0 to 50.0 [Technical Information; Characteristics and Use of Si APD (Avalanche Photodiode), 2018]. The numerically calculated ENF of Si flat nano-APDs is found to be remaining within the range of 3.4–14.9 for the same range of multiplication gain, which is observed to be in close agreement with the measured ENF values. Close agreement between the calculated and experimental data validates the simulation methodology adopted by the authors in this paper. But so far as authors' knowledge is concerned, no experimental report on ENF versus gain characteristics of Si~3C-SiC MQB nano-APDs are available in literature. That is why the numerically calculated ENF values of the MQB nano-APDs could not be compared with the experimental results. However, the simulation results suggest that very small ENF, typically 1.58–2.91 is achievable in MQB APDs for the multiplication gain range of 2.0–20.0 when the number of QBs is kept $N_b = 5$.

5 Time and frequency responses

The 1D model of the MQB APD structure under ITPS configuration is shown in Figure 11.

Initially the total injected electron and hole photo-generated current densities containing both drift and diffusion components have been calculated by considering a rectangular shaped incident optical flux density pulse having finite pulse width. Then, the total multiplied electron and hole current densities as functions of both space and time have been obtained from the simultaneous solution of the fundamental transport equations subject to appropriate boundary conditions imposed at the depletion layer edges. The space integration over the entire device length of the sum of electron and hole currents provides the pulse current response in time domain. Finally, the frequency domain of the current response has been obtained via the Fourier transform of time domain of pulse current response.

The incident optical pulse having rectangular pulse shape is assumed to incident on the p^+-side of the APD. The unit rectangular optical pulse has the mathematical form:

$$p_{rect}(t) = u(t) - u\left(t - \Delta_{pl}\right) \tag{80}$$

where Δ_{pl} is the duration of the pulse and $u(t)$ is the Heaviside step function of time given by:

$$\left.\begin{aligned} u(t) &= 1, \quad t \geq 0 \\ &= 0, \quad t < 0 \end{aligned}\right\} \tag{81}$$

Therefore, the incident time varying photon flux density of wavelength λ is given by:

$$\Phi_{(opt)}^{(\lambda)}(t) = \Phi_0^{(\lambda)} p_{rect}(t) \tag{82}$$

where $\Phi_0^{(\lambda)}$ is the magnitude of incident photon flux density at $t = 0$; it is given by:

$$\Phi_0^{(\lambda)} = \left\{\frac{P_{opt}\left(1 - R(\lambda)\right)\lambda}{A_i hc}\right\} \tag{83}$$

where P_{opt} is the incident optical power, A_i is the illumination area, $h = 6.62\times10^{-34}$ J s is the Planck's constant, $c = 3.0\times10^{8}$ m s^{-1} is the velocity of light in vacuum, $R(\lambda)$ is the reflectance of Si at p^+-side which is a function of wavelength.

Now, the drift photocurrent density in ITPS configuration can be evaluated by using the similar method as earlier in this paper. The time varying electron and hole drift photocurrent densities are obtained as:

$$\begin{aligned} J_{n(opt\_drt)}^{(\lambda)}(t) &= J_{p(opt\_drt)}^{(\lambda)}(t) \\ &= -q\Phi_{(opt)}^{(\lambda)}(t) e^{-\alpha_{p(inb)}^{(Si)}(\lambda,|N_A|)W_p} \left(\int_{x=0}^{x=W_i} \alpha(\lambda, x) e^{-\alpha(\lambda,x)x} dx \right) \end{aligned} \tag{84}$$

where $q = 1.6 \times 10^{-19}$ C is the unit electronic charge, $\alpha(\lambda,x)$ is the space dependent absorption coefficient in the MQB APD structure as depicted in the equation (6),

$\alpha_{p(inb)}^{(Si)}(\lambda,|N_A|)$ is the absorption coefficient of Si due to interband transitions at p^+-region having doping density N_A, at 300 K temperature. On the other hand, the electron and hole diffusion photocurrent densities can be obtained by solving the carrier space and time dependent carrier continuity equations for ITPS structure by following the method described in the Section 3 of this paper. Those are obtained as:

$$
\begin{aligned}
J_{n(opt\_diff)}^{(\lambda)}(t) = qD_n^{(Si)} & \left[\left(\frac{\Phi_{(opt)}^{(\lambda)}(t)\left(\alpha_{p(inb)}^{(Si)}\left(\lambda,|N_A|\right)\right)^2\left(L_n^{(Si)}\right)^2}{D_n^{(Si)}\left\{1-\left(\alpha_{p(inb)}^{(Si)}\left(\lambda,|N_A|\right)\right)^2\left(L_n^{(Si)}\right)^2\right\}} \right) \right. \\
& -\left(\frac{1}{L_n^{(Si)}\sinh\left(\frac{W_p}{L_n^{(Si)}}\right)} \right)\left\{ n_{p0}\left(1-\cosh\left(\frac{W_p}{L_n^{(Si)}}\right)\right) \right. \\
& \left. \left. +\left(\frac{\Phi_{(opt)}^{(\lambda)}(t)\alpha_{p(inb)}^{(Si)}\left(\lambda,|N_A|\right)\left(L_n^{(Si)}\right)^2}{D_n^{(Si)}\left\{1-\left(\alpha_{p(inb)}^{(Si)}\left(\lambda,|N_A|\right)\right)^2\left(L_n^{(Si)}\right)^2\right\}} \right)\left(\begin{matrix} e^{\alpha_{p(inb)}^{(Si)}(\lambda,|N_A|)W_p} \\ -\cosh\left(\frac{W_p}{L_n^{(Si)}}\right) \end{matrix} \right) - n_p^{(\lambda)}(0,t) \right\} \right]
\end{aligned}
\tag{85}
$$

$$
\begin{aligned}
& J_{p(opt\_diff)}^{(\lambda)}(t) \\
& = qD_p^{(Si)} \left[\left(\frac{\Phi_{(opt)}^{(\lambda)}(t)\left(\alpha_{n(inb)}^{(Si)}\left(\lambda,|N_D|\right)\right)^2\left(L_p^{(Si)}\right)^2}{D_p^{(Si)}\left\{1-\left(\alpha_{n(inb)}^{(Si)}\left(\lambda,|N_D|\right)\right)^2\left(L_p^{(Si)}\right)^2\right\}} \right) e^{-\left(\begin{matrix} \alpha_{p(inb)}^{(Si)}(\lambda,|N_A|)W_p+\alpha_{n(inb)}^{(Si)}(\lambda,|N_D|)W \\ +\left(\alpha_{\pi(insb)}^{(Si)}(\lambda,|N_i|)+\alpha_{\pi(inb)}^{(Si)}(\lambda,|N_i|)\right)N_wW_w \\ +\alpha_{\pi(inb)}^{(3C-SiC)}(\lambda,|N_i|)N_bW_b \\ +\alpha_{\pi(inb)}^{(Si)}(\lambda,|N_i|)(W_i-N_bW_b-N_wW_w) \end{matrix} \right)} \right. \\
& +\left(\frac{1}{L_p^{(Si)}\sinh\left(\frac{W_n}{L_p^{(Si)}}\right)} \right)\left\{ p_{n0}\left(1+\cosh\left(\frac{W_n}{L_p^{(Si)}}\right)\right) \right. \\
& \left. \left. +\left(\frac{\Phi_{(opt)}^{(\lambda)}(t)\alpha_{n(inb)}^{(Si)}\left(\lambda,|N_D|\right)\left(L_p^{(Si)}\right)^2}{D_p^{(Si)}\left\{ \begin{matrix} 1 \\ -\left(\alpha_{n(inb)}^{(Si)}\left(\lambda,|N_D|\right)\right)^2\left(L_p^{(Si)}\right)^2 \end{matrix} \right\}} \right) e^{-\left(\begin{matrix} \alpha_{p(inb)}^{(Si)}(\lambda,|N_A|)W_p \\ +\alpha_{n(inb)}^{(Si)}(\lambda,|N_D|)W \\ +\left(\begin{matrix} \alpha_{\pi(insb)}^{(Si)}(\lambda,|N_i|) \\ +\alpha_{\pi(inb)}^{(Si)}(\lambda,|N_i|) \end{matrix} \right)N_wW_w \\ +\alpha_{\pi(inb)}^{(3C-SiC)}(\lambda,|N_i|)N_bW_b \\ +\alpha_{\pi(inb)}^{(Si)}(\lambda,|N_i|)(W_i-N_bW_b \\ -N_wW_w) \end{matrix} \right)} \left(\begin{matrix} e^{-\alpha_{n(inb)}^{(Si)}(\lambda,|N_D|)(W_i+W_n)} \\ -\cosh\left(\frac{W_n}{L_p^{(Si)}}\right) \end{matrix} \right) \right. \\
& \left. -p_n^{(\lambda)}(0,t) \right\} \Bigg]
\end{aligned}
\tag{86}
$$

Now, the total time varying electron and hole photocurrent densities can be obtained by summing their drift and diffusion components; those are given by:

$$
\left.
\begin{aligned}
J_{n(opt)}^{(\lambda)}(t) &= J_{n(opt\_drt)}^{(\lambda)}(t) + J_{n(opt\_diff)}^{(\lambda)}(t) \\
J_{p(opt)}^{(\lambda)}(t) &= J_{p(opt\_drt)}^{(\lambda)}(t) + J_{p(opt\_diff)}^{(\lambda)}(t)
\end{aligned}
\right\}
\tag{87}
$$

The equation (87) provide the time varying photocurrent densities (both electron and hole components respectively) injected into the device through p^+-side due to absorption of photons of wavelength λ from the optical pulse [equation (82)] incident on the p^+-side of the MQB APD structure under ITPS configuration. The electric field eventually sweep the electrons towards n^+-side through the π-region, which are further multiplied due to the impact ionisation phenomena near the π-side of the π-n^+ junction (high field region). However, the photo-generated holes do not get the opportunity to be multiplied by the above-mentioned phenomena, because those are swept out of the device in the opposite direction through p^+-side. The current response of the device due to the application of such optical pulse at the p^+-side can be obtained from the simultaneous solution of both time and space dependent fundamental device equations such as Poisson's equation, carrier-continuity equations and current density equations subject to the appropriate boundary conditions imposed at the depletion layer edges of the device, i.e., at $x = 0$ and $x = W_i$. The above-mentioned transport equations are given by:

$$\frac{\partial}{\partial x}\left(\varepsilon(x)\frac{\partial V^{(\lambda)}(x,t)}{\partial x}\right) = q\begin{pmatrix} p_p^{(\lambda)}(x,t) \\ -n_n^{(\lambda)}(x,t) \\ +N(x) \end{pmatrix} \tag{88}$$

$$\frac{\partial J_n^{(\lambda)}(x,t)}{\partial t} + \left(\frac{1}{q}\right)\frac{\partial J_n^{(\lambda)}(x,t)}{\partial x} = \begin{pmatrix} G_{n(AV)}^{(\lambda)}(x,t) \\ +G_{n(BBT)}^{(\lambda)}(x,t) \\ +G_{n(TAT)}^{(\lambda)}(x,t) \\ -R_n(x,t) \end{pmatrix} \tag{89}$$

$$\frac{\partial J_p^{(\lambda)}(x,t)}{\partial t} - \left(\frac{1}{q}\right)\frac{\partial J_p^{(\lambda)}(x,t)}{\partial x} = \begin{pmatrix} G_{p(AV)}^{(\lambda)}(x,t) \\ +G_{p(BBT)}^{(\lambda)}(x,t) \\ +G_{p(TAT)}^{(\lambda)}(x,t) \\ -R_p(x,t) \end{pmatrix} \tag{90}$$

$$J_n^{(\lambda)}(x,t) = -\left(\begin{matrix} qn_n^{(\lambda)}(x,t)\mu_n(x)\dfrac{\partial V^{(\lambda)}(x,t)}{\partial x} \\ +qD_n(x)\dfrac{\partial n_n^{(\lambda)}(x,t)}{\partial x} \end{matrix}\right) + J_{n(opt)}^{(\lambda)}(t)\Big| \tag{91}$$

$$J_p^{(\lambda)}(x,t) = -\left(\begin{matrix} qp_p^{(\lambda)}(x,t)\mu_p(x)\dfrac{\partial V^{(\lambda)}(x,t)}{\partial x} \\ -qD_p(x)\dfrac{\partial p_p^{(\lambda)}(x,t)}{\partial x} \end{matrix}\right) + J_{p(opt)}^{(\lambda)}(t) \tag{92}$$

where $V^{(\lambda)}(x,\ t)$, $J_n^{(\lambda)}(x,t), J_p^{(\lambda)}(x,t), n_n^{(\lambda)}(x,t)$ and $p_p^{(\lambda)}(x,t)$ are the time and space dependent electric potential, electron and hole current densities and electron and hole densities, which are the unknown variable, obtainable from the simultaneous solutions of the partial differential equations given in the equations (88)–(92); the parameters $\mu_{n,p}(x)$,

$D_{n,p}(x)$ and $\varepsilon(x)$ are space dependent electron and hole mobility, diffusivity and permittivity of the MQB APD structure, which are defined in Section 3. The field dependent expressions of avalanche generation rate $(G^{(\lambda)}_{n,p(AV)}(x,t))$, band-to-band tunnelling generation rate $(G^{(\lambda)}_{n,p(BBT)}(x,t))$, trap assisted tunnelling generation rate $(G^{(\lambda)}_{n,p(TAT)}(x,t))$ and Shockley-Read-Hall recombination rate $(R^{(\lambda)}_{n,p}(x,t))$ of electrons and holes have already been reported earlier (Ghosh et al., 2017). Now, the time varying electric potential and current density boundary conditions to be imposed at $x = 0$ and $x = W_i$ in order to obtain the simultaneous solution of the equations (88)–(92) have been discussed in the next paragraph.

Figure 11 1D model of reverse biased MQB nano-APD (having typically four QBs) under ITPS configuration

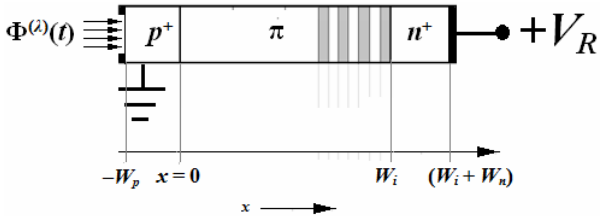

The time varying boundary conditions for the electric potential are given by:

$$\left.\frac{\partial V^{(\lambda)}(x,t)}{\partial x}\right|_{x=0} = \left.\frac{\partial V^{(\lambda)}(x,t)}{\partial x}\right|_{x=W_i} = 0 \tag{93}$$

On the other hand, the time varying boundary conditions for the normalised current density parameter:

$$NJ^{(\lambda)}(x,t) = \left(\frac{J_p^{(\lambda)}(x,t) - J_n^{(\lambda)}(x,t)}{J_p^{(\lambda)}(x,t) + J_n^{(\lambda)}(x,t)}\right) \tag{94}$$

At $x = 0$ and $x = W_i$ are given by:

$$\left.\begin{aligned} NJ^{(\lambda)}(x=0,t) &= \left(1 - \frac{2J_n^{(\lambda)}(x=0,t)}{J_p^{(\lambda)}(x=0,t) + J_n^{(\lambda)}(x=0,t)}\right) \\ NJ^{(\lambda)}(x=W_i,t) &= \left(\frac{2J_p^{(\lambda)}(x=W_i,t)}{J_p^{(\lambda)}(x=W_i,t) + J_n^{(\lambda)}(x=W_i,t)} - 1\right) \end{aligned}\right\} \tag{95}$$

The simultaneous solutions of equations (88)–(92) are obtained subject to the boundary conditions given in the equations (93)–(95) by using FDM with 500 space steps within $x = -W_p$ to $x = (W_i + W_n)$ and 500 time steps within the time interval $t = 0$ to $t = \beta\Delta_{pl}$; where β is any positive integer ($\beta > 1$). Once $J_n^{(\lambda)}(x,t)$ and $J_p^{(\lambda)}(x,t)$ are determined, the total time varying current induced in the external circuit that results from the electron and hole transport within the device is given by:

$$I^{(\lambda)}(t) = \left(\frac{A_j}{W_n + W_i + W_p}\right) \int_{x=-W_p}^{x=W_i+W_n} \left(J_n^{(\lambda)}(x,t) + J_p^{(\lambda)}(x,t)\right) dx \tag{96}$$

Fourier transform of $I^{(\lambda)}(t)$ will provide the current response in frequency domain, which is given by:

$$I^{(\lambda)}(f) = \int_{-\infty}^{+\infty} I^{(\lambda)}(t) e^{-j2\pi ft} dt \tag{97}$$

The Fourier transform of $I^{(\lambda)}(t)$ (where $I^{(\lambda)}(t) \leftrightarrow I^{(\lambda)}(f)$) is obtained via fast Fourier transform (FFT) algorithm with sampling frequency $f_s > 10/\Delta_{pl}$ in the MATLAB environment.

Figure 12 Optical pulses having different pulse widths and corresponding response currents as functions of time in, (a)–(c) Si flat nano-APD (d)–(f) Si~3-SiC MQB nano-APD under ITPS configuration (see online version for colours)

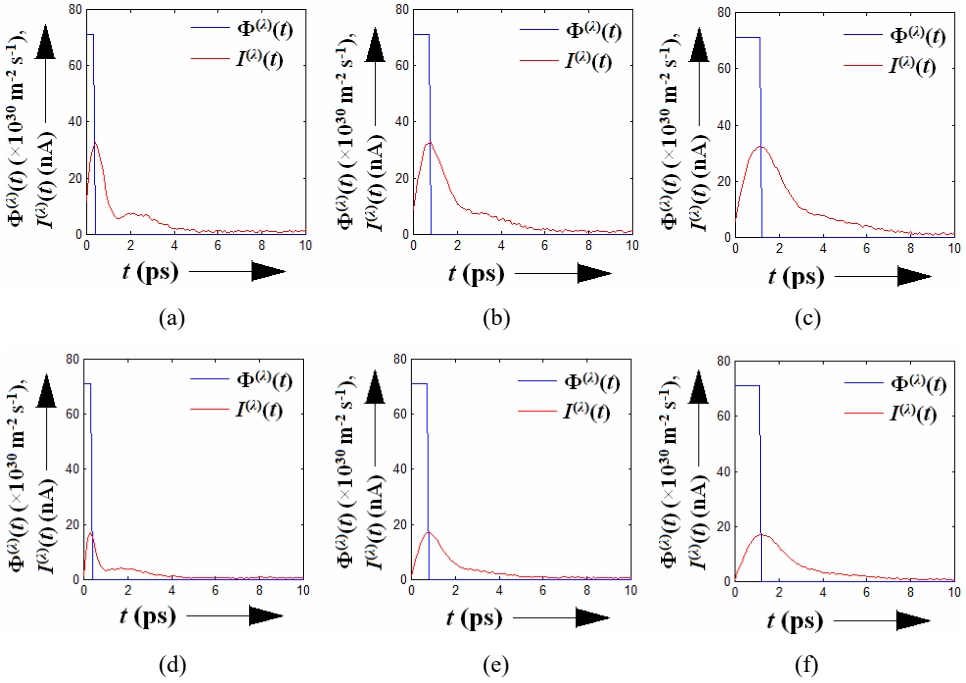

Note: The first sharp peak of the current response corresponds to the first arrival of injected electrons and the subsequent peaks are due to arrivals of secondary generations of electrons and holes.

Time and frequency responses of MQB nano-APDs based on Si~3C-SiC heterostructures under ITPS configuration have been investigated by using the simulation methodology described in the earlier section. Optical pulses having pulse widths Δ_{pl} = 0.4, 0.8 and 1.2 ps of 850 nm wavelength have been used as the input and the corresponding current responses of flat Si nano-APD as well as Si~3C-SiC MQB nano-APD having five QBs made of 3C-SiC (each of thickness 5 nm and separated by 5 nm QWs made of Si) under

ITPS configuration have been shown in Figures 12(a)–12(f). Figures 12(a)–12(f) show that the entire current responses are clearly non-exponential in nature. However, the tails of those are exponential in nature. The current responses have multiple peaks; the first and the major peak is corresponding to the original injected electrons and subsequent peaks are corresponding to the secondary generation of electrons and holes due to the impact ionisation phenomenon within the high field multiplication region near the π-n^+ junction. The width of the current responses are limited to 4.7 and 3.1 ps for the input optical pulse of width 0.4 ps in Si nano-APD as well as Si~3C-SiC MQB nano-APD respectively. The cause of faster time response of MQB APD as compared to flat Si APD is due to the greater ionisation rate $(\zeta_n^{(3C-SiC)} > \zeta_n^{(Si)})$ and saturation drift velocity $(v_{sn}^{(3C-SiC)} > v_{sn}^{(Si)})$ of electrons in 3C-SiC than the Si at room temperature (300 K) (Rajkanan et al., 1979; Spitzer and Fan, 1957; Hara and Nishi, 1966; Solangi and Chaudry, 1992; Mukherjee and Das, 2014; Manasreh, 2005; Ghosh et al., 2017; Costato and Reggiani, 1970; Selberherr, 1984; Weisbuch and Vinter, 1991; Doudlas and Yuan, 1987; Christodoulou, 2009; Stern, 1970; Grant, 1973; Bellotti et al., 1999; Mickevicius and Zhao, 1998; Canali et al., 1971; IOFFE, 2019; Zeghbroeck, 2011; May, 2005; Yan-Kun et al., 2012). As compared with flat Si APD of same gain, MQB APD has much faster time response and lower noise factor because of the narrower avalanche zone width and localised ionisation layers in the later one.

The time response of nano-APDs having different number of QBs [N_b = 0 (flat Si APD), 3 and 5] for the input optical pulse of pulse width 0.4 ps have been shown in Figure 13. It is important to observe from Figure 13 as well as Figures 12(a)–12(f) that the initial peak of the current response decreases significantly with the increase of number of QBs; however, the tail of the current response decays with much faster rate in MQB APDs having greater number of QBs. Therefore, the incorporation of QBs in the multiplication region of nano-APDs improves the time response, excess noise characteristics, reduces the dark current (Acharyya and Ghosh, 2017); however, the spectral response of the device is deteriorated up to near-infrared range. But MQB APDs are capable of detecting up to mid-infrared wavelengths (up to 4,000 nm); where the spectral response of flat Si APD is limited up to near infrared (up to 1,100 nm) range. The normalised frequency response of flat Si APD and Si~3C-SiC MQB nano-APDs having 0, 3 and 5 QBs respectively have been obtained from the Fourier transform of corresponding time responses to 0.4 ps optical pulse of wavelength 850 nm; those are shown in Figure 14. The 3 dB upper cut-off frequencies of the diodes are obtained to be f_{u0} = 68.63 GHz, f_{u3} = 74.63 GHz and f_{u5} = 82.64 GHz (corresponding 3 dB bandwidths can be calculated from $BW_{N_b} = \left(f_{uN_b} - f_{lN_b}\right)$; where $f_{lN_b} = 0$). It is obvious that shorter the width of the time response, broader the bandwidth. Therefore, significantly greater 3 dB bandwidth can be achieved in Si nano-APDs by incorporating QBs made of wider bandgap material 3C-SiC within the multiplication region near the π-n^+ junction. It is noteworthy from Figure 14 that around 14 GHz greater bandwidth can be achieved by incorporating 5 nm wide 5 number of 3C-SiC QBs in Si nano-APD mutually separated by 5 nm QWs made of Si as compared to the conventional flat Si nano-APD.

Figure 13 Pulse response currents as functions of time in Si flat nano-APD and Si~3-SiC MQB nano-APDs having 3 and 5 numbers of QBs; all the devices have been illuminated under ITPS configuration (see online version for colours)

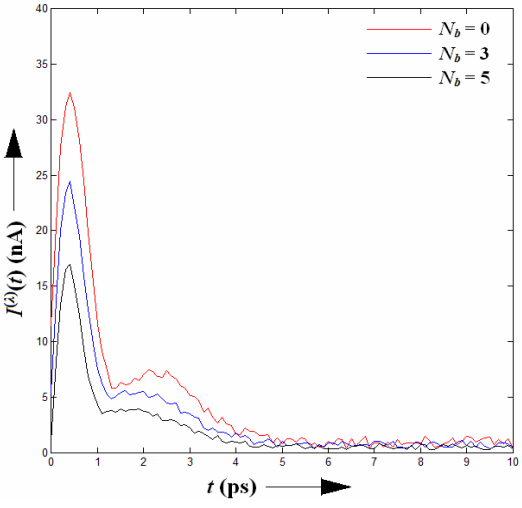

Figure 14 Frequency response of Si flat nano-APD and Si~3-SiC MQB nano-APDs having 3 and 5 numbers of QBs; all the devices have been illuminated under ITPS configuration (see online version for colours)

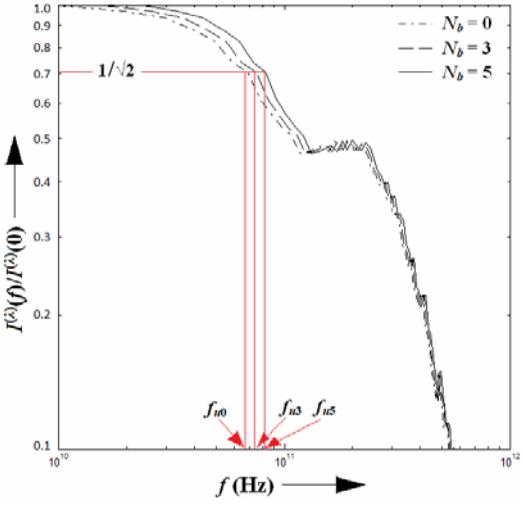

6 Conclusions

The comprehensive simulation models developed by the authors have been used to simulate the spectral response, excess noise characteristics, time and frequency responses of Si~3C-SiC MQB nano-APD structures within a wide range of wavelengths (200–4,000 nm). Both types of illumination configurations such as ITNS and ITPS have

been simulated and ITPS configuration is found to be the preferable one due its better spectral response characteristics within 200–4,000 nm wavelength range as compared to its ITNS counterpart. Capability of longer wavelength detection of the proposed MQB nano-APDs makes those extremely versatile candidates for the potential applications in deep space astronomical observations. The excess noise characteristics as well as the time and frequency response of MQB nano-APDs based on Si~3C-SiC material system will be discussed in the succeeding parts of this paper in this journal. The ENF of the MQB APDs have been calculated for different number of QBs and those are compared with the ENF of Si flat conventional APDs of similar dimensions. It is observed that the use of QBs leads to significant reduction in ENF of the APDs under similar biasing and illumination conditions. The enhanced ratio of hole to electron ionisation rates in MQB structures as compared to the bulk Si APD structure has been found to be the primary cause of improvement in the noise performance of the MQB nano-APDs. The time and frequency responses of MQB APDs based on Si~3C-SiC material system have also been investigated by the authors. A very narrow-width rectangular pulse of pulse-width of 0.4 ps has been used as the input optical pulse having 850 nm wavelength incident on the p^+-side of the MQB APD structures and corresponding current response has been calculated by using a simulation method developed by the authors; finally the frequency response of the devices are obtained via the Fourier transform of the corresponding pulse current response in time domain. Simulation results show that MQB nano-APDs possess significantly faster time response and wider frequency response as compared to the flat Si nano-APDs under similar operating conditions.

The entire study presented in this paper suggests that the Si~3C-SiC MQB nano-APDs provide:

1 smaller dark current

2 wider spectral response

3 smaller excess noise

4 faster time response

5 greater bandwidth as compared to the flat Si nano-APD under similar operating conditions.

References

Acharyya, A. and Ghosh, S. (2017) 'Dark current reduction in nano-avalanche photodiodes by incorporating multiple quantum barriers', *International Journal of Electronics*, Vol. 104, No. 12, pp.1957–1973.

Arthur, J.R. (2002) 'Molecular beam epitaxy', *Surface Science*, Vol. 500, Nos. 1–3, pp.189–217.

Assefa, S., Xia, F.N., Green, W.M.J., Schow, C.L., Rylyakov, A.V. and Vlasov, Y.A. (2010) 'CMOS-integrated optical receivers for on-chip interconnects', *IEEE J. Sel. Topics Quant. Electron.*, Vol. 16, No. 5, pp.1376–1385.

Bellotti, E., Nilsson, H.E., Brennan, K.F. and Ruden, P.P. (1999) 'Ensemble Monte Carlo calculation of hole transport in bulk 3C-SiC', *J. Appl. Phys.*, Vol. 85, No. 6, pp.3211–3217.

Brennan, K.F. and Haralson, J. (2000) 'Superlattice and multiquantum well avalanche photodetectors: physics, concepts and performance', *Superlattices and Microstructures*, Vol. 28, No. 2, pp.77–104.

Britvitch, I. et al. (2004) 'Avalanche photodiodes now and possible developments', *NIM A*, Vol. 535, Nos. 1–2, pp.523–527.

Canali, C., Ottaviani, G. and Quaranta, A.A. (1971) 'Drift velocity of electrons and holes and associated anisotropic effects in silicon', *Journal of Physics and Chemistry of Solids*, Vol. 32, No. 8, pp.1707–1720.

Capasso, F., Tsang, W.T. and Williams, G.F. (1983) 'Staircase solid-state photomultiplier and avalanche photodiodes with enhanced ionization rates ratio', *IEEE Transactions of Electron Devices*, Vol. 30, No. 4, pp.381–390.

Chen, Y.M., Wang, Z.G., Fan, X.N., Wang, H. and Li, W. (2013) 'A 38 Gb/s to 43 Gb/s monolithic optical receiver in 65 nm CMOS technology', *IEEE Trans. Circuits Syst.*, Vol. 60, No. 12, pp.3173–3181.

Chin, R., Holonyak, N., Stillman, G.E., Tang, J.Y. and Hess, K. (1980) 'Impact ionisation in multilayered heterojunction structures', *Electronic Letters*, Vol. 16, No. 12, pp.467–468.

Christodoulou, N.S. (2009) 'An algorithm using Runge-Kutta methods of orders 4 and 5 for systems of ODEs', *International Journal of Numerical Methods and Applications*, Vol. 2, No. 1, pp.47–57.

Costato, M. and Reggiani, L. (1970) 'Temperature-dependence of the combined effective mass of holes in silicon', *Lettere Al Nuovo Cimento*, Vol. 3, No. 8, pp.239–245.

CW Tunable Ti:Sapphire Laser 3900S (2018) [online] http://www.newport.com/3900S-CW-Tunable-Ti-Sapphire-Laser/368139/1033/info.aspx#tab_Specifications (accessed December 2018).

Dong, Y., Wang, W., Lee, S.Y., Lei, D., Gong, X., Loke, W.K., Yoon, S.F., Liang, G. and Yeo, Y.C. (2016) 'Germanium-tin multiple quantum well on silicon avalanche photodiode for photodetection at two micron wavelength', *Semiconductor Science and Technology*, Vol. 31, No. 9, pp.095001-1-10.

Doudlas, J. and Yuan, Y. (1987) *Finite Difference Method for the Transient Behavior of a Semiconductor Device*, IMA Preprint Series # 286, pp.1–20.

Fissel, A., Kaiser, U., Schröte, B., Richter, W. and Bechstedt, F. (2001) 'MBE growth and properties of SiC multi-quantum well structures', *Applied Surface Science*, Vol. 184, Nos. 1–4, pp.37–42.

Ghosh, M., Ghosh, S. and Acharyya, A. (2017) 'Self-consistent quantum drift-diffusion model for multiple quantum well IMPATT diodes', *Journal of Computational Electronics*, Vol. 15, No. 4, pp.1370–1387.

Grant, W.N. (1973) 'Electron and hole ionization rates in epitaxial silicon at high electric fields', *Solid State Electronics*, Vol. 16, No. 10, pp.1189–1203.

Hara, H. and Nishi, Y. (1966) 'Free carrier absorption in p-type silicon', *Journal of the Physical Society of Japan*, Vol. 21, No. 6, p.1222.

Holonyak, N., Kolbas, R.M., Dupuis, R.D. and Dapkus, P.D. (1980) 'Quantum-well heterostructure lasers', *IEEE Journal of Quantum Electronics*, Vol. 16, No. 2, pp.170–186.

IOFFE (2019) *Electronic Archive: New Semiconductor Materials, Characteristics and Properties* [online] http://www.ioffe.ru/SVA/NSM/Semicond/index.html (accessed January 2019).

Joo, J., Jang, K.S., Kim, S.H. et al. (2005) 'Silicon photonic receiver and transmitter operating up to 36 Gb/s for λ~1550 nm', *Opt. Express*, Vol. 23, No. 9, pp.12232–12243.

Kandaswam, P.K., Machhadani, H., Bellet-Amalric, E., Nevou, L., Tchernycheva, M., Lahourcade, L., Julien, F.H. and Monroy, E. (2009) 'Strain effects in GaN/AlN multi-quantum-well structures for infrared optoelectronics', *Microelectronics Journal*, Vol. 40, No. 2, pp.336–338.

Manasreh, O. (2005) *Semiconductor Heterojunctions and Nanostructures*, pp.210–216, McGraw-Hill, New York.

Masudy-Panah, S. (2011) 'Nonlocal analysis to study of the impact ionization and avalanche characteristics of deep submicron Si devices', *Solid State Communications*, Vol. 151, No. 8, pp.610–614.

Masudy-Panah, S. and Moravvej-Farshi, M.K. (2010) 'An analytic approach to study the effects of optical phonon scattering loss on the characteristics of avalanche photodiodes', *IEEE Journal of Quantum Electronics*, Vol. 46, No. 4, pp.533–540.

Masudy-Panah, S. and Tikkiwal, V.A. (2015) 'Velocity enhancement in APDs with sub-100-nm multiplication region', *Optics Communications*, Vol. 346, No. 1, pp.167–171.

Masudy-Panah, S., Moravvej-Farshi, M.K. and Jalali, M. (2009) 'Temperature dependent characteristics of submicron GaAs avalanche photodiodes obtained by a nonlocal analysis', *Optics Communications*, Vol. 282, No. 1, pp.3630–3636.

May, C.P. (2005) *Impact Ionization Rate Calculations for Device Simulation*, ETH, Eidgenössische Technische Hochschule Zürich, Integrated Systems Laboratory.

McIntyre, R.J. (1966) 'Multiplication noise in uniform avalanche diodes', *IEEE Trans. Electron Devices*, Vol. 13, No. 1, pp.164–168.

Mickevicius, R. and Zhao, J.H. (1998) 'Monte Carlo study of electron transport in SiC', *J. Appl. Phys.*, Vol. 83, No. 6, pp.3161–3167.

Mukherjee, K. and Das, N.R. (2014) 'Absorption coefficient in a MQW intersubband photodetector with non-uniform doping density & layer distribution', *Progress in Electromagnetics Research M*, Vol. 38, No. 1, pp.193–201.

Othman, M.A., Taib, S.N., Husain, M.N. and Napiah, Z.A.F.M. (2004) 'Reviews on avalanche photodiode for optical communication technology', *ARPN Journal of Engineering and Applied Sciences*, Vol. 9, No. 1, pp.35–44.

Pan, Q., Hou, Z.X., Li, Y., Poon, A.W. and Yue, C.P. (2014) 'A 0.5-V p-well/deep n-well photodetector in 65-nm CMOS for monolithic 850-nm optical receivers', *IEEE Photon. Technol. Lett.*, Vol. 26, No. 12, pp.1184–1187.

Pansarat, J. (1997) 'Avalanche photodiodes for particle detection', *Nucl. Instr. Meth. A*, Vol. 389, Nos. 1–2, pp.186–186.

PerkinElmer (2018) *Silicon Avalanche Photodiodes* [online] http://www.perkinelmer.com/CMSResources/Images/44-3477DTS_C30902.pdf (accessed December 2018).

Qamar, A., Tanner, P., Dao, D.V., Phan, H.P. and Dinh, T. (2014) 'Electrical properties of p-type 3C-SiC/Si heterojunction diode under mechanical stress', *IEEE Electron Device Letters*, Vol. 35, No. 12, pp.1293–1295.

Rajkanan, K., Singh, R. and Shewchun, J. (1979) 'Absorption coefficient of silicon for solar cell calculations', *Solid-State Electronics*, Vol. 22, No. 9, pp.793–795.

Renker, D. (2002) 'Properties of avalanche photodiodes for applications in high energy physics, astrophysics, and medical imaging', *NIM A*, Vol. 486, Nos. 1–2, pp.164–169.

Schweighart, A., Vyas, H.P., Borrego, J.M. and Gutmann, R.J. (1978) 'Avalanche diode structure suitable for microwave-optical interaction', *Solid-State Electron*, Vol. 21, No. 9, pp.1119–1121.

Selberherr, S. (1984) *Analysis and Simulation of Semiconductor Devices*, Springer Verlag, Wien.

Shichuo, H., Kolbas, R.M., Holonyak, N., Dupuis, R.D. and Dapkus, P.D. (1978) 'Carrier collection in a semiconductor quantum well', *Solid State Communication*, Vol. 27, No. 10, pp.1029–1032.

Solangi, A. and Chaudry, M.I. (1992) 'Absorption coefficient of beta--SiC grown by chemical vapor deposition', *J. Mater. Res.*, Vol. 7, No. 3, pp.539–541.

Spitzer, W. and Fan, H.Y. (1957) 'Infrared absorption in n-type silicon', *Phys. Rev.*, Vol. 108, No. 2, pp.268–271.

Stern, F. (1970) 'Iteration methods for calculating self-consistent fields in semiconductor inversion layers', *Journal of Computational Physics*, Vol. 6, No. 1, pp.56–67.

Tanner, P., Iacopi, A., Phan, H.P., Dimitrijev, S., Hold, L., Chaik, K., Walker, G., Dao, D.V. and Nguyen, N.T. (2017) 'Excellent rectifying properties of the n-3C-SiC/p-Si heterojunction subjected to high temperature annealing for electronics, MEMS, and LED applications', *Nature Scientific Reports*, Vol. 7, No. 1, pp.17734-1-11.

Technical Information; Characteristics and Use of Si APD (Avalanche Photodiode) (2018) [online] http://neutron.physics.ucsb.edu/docs/Characteristics_and_use_of_SI_APD.pdf (accessed December 2018).

Teich, M.C., Matsuo, K. and Saleh, B.E.A. (1996) 'Excess noise factors for conventional and supperlattice avalanche photodiodes and photomultiplier tube', *IEEE Journal of Quantum Electronics*, Vol. 22, No. 8, pp.1184–1193.

Uemura, H., Kurita, Y. and Furuyama, H. (2006) '12.5 Gb/s optical driver and receiver ICs with double-threshold AGC for SATA out-of-band transmission', *IEEE J. Solid-State Circuits*, Vol. 51, No. 7, pp.1–10.

van Vliet, K.M., Friedmann, A. and Rucker, L.M. (1979) 'Theory of carrier multiplication and noise in avalanche devices – part II: two-carrier processes', *IEEE Transactions on Electron Devices*, Vol. 26, No. 5, pp.752–764.

Vyas, H.P., Gutmann, R.J. and Borrego, J.M. (1977) 'Leakage current enhancement in IMPATT oscillator by photoexcitation', *Electron. Lett.*, Vol. 13, No. 7, pp.189–190.

Vyas, H.P., Gutmann, R.J. and Borrego, J.M. (1979) 'Effect of hole versus electron photocurrent on microwave-optical interactions in Impatt oscillators', *IEEE Transactions on Electron Devices*, Vol. 26, No. 3, pp.232–234.

Wang, W., Wang, L., Li, M., Li, Q., Kang, J., Luo, Y. and Zhang, J. (2018) 'Analysis of negative differential conductance in a GaN.AlN multi-quantum-well avalanche photodiode', *Proceedings of SPIE, Optical Sensing, Imaging, and Photon Counting: From X-Rays to THz*, San Diego, California, USA, Vol. 10729.

Wêgrzecka, I., Wêgrzecki, M., Grynglas, M., Bar, J., Uszyñski, A., Grodecki, R., Grabiec, P., Krzemiñski, S. and Budzyñski, T. (2004) 'Design and properties of silicon avalanche photodiodes', *Opto-Electronics Review*, Vol. 12, No. 1, pp.95–104.

Weisbuch, C. and Vinter, B. (1991) *Quantum Semiconductor Structures*, Academic Press Inc., New York.

Yang, L., Dzhosyuk, S.N., Gabrielse, J.M., Huffman, P.R., Mattoni, C.E.H., Maxwell, S.E., McKinsey, D.N. and Doyle, J.M. (2003) 'Performance of a large-area avalanche photodiode at low temperature for scintillation detection', *Nuclear Instruments and Methods in Physics Research A*, Vol. 508, No. 3, pp.388–393.

Yan-Kun, D., Xin, Q., Hai-Bo, J., Mao-Sheng, C., Zahid, U. and Zhi-Ling, H. (2012) 'First principle study of the electronic properties of 3C-SiC doped with different amounts of Ni', *Chin. Phys. Lett.*, Vol. 29, No. 7, pp.077701-1-4.

Youn, J.S., Lee, M.J., Park, K.Y., Kim, W.S. and Choi, W.Y. (2015) 'Low-power 850 nm optoelectronic integrated circuit receiver fabricated in 65 nm complementary metal-oxide semiconductor technology', *IET Circuits Devices Syst.*, Vol. 9, No. 3, pp.221–226.

Zeghbroeck, B.V. (2011) *Principles of Semiconductor Devices*, Colorado Press, USA.